nature communications

Article

https://doi.org/10.1038/s41467-025-65070-x

Extreme properties of a compact and massive accreting black hole host in the first 500 Myr

Received: 29 November 2024

Accepted: 6 October 2025

Published online: 19 November 2025

Check for updates

Roberta Tripodi[1,2] ✉, Nicholas Martis[1], Vladan Markov[1], Maruša Bradač[1], Fabio Di Mascia[3], Vieri Cammelli[4], Francesco D'Eugenio[5,6], Chris Willott[7], Mirko Curti[8], Maulik Bhatt[3], Simona Gallerani[3], Gregor Rihtaršič[1], Jasbir Singh[9], Gaia Gaspar[10], Anishya Harshan[1], Jon Judež[1], Rosa M. Merida[10], Guillaume Desprez[10,11], Marcin Sawicki[10], Ilias Goovaerts[12], Adam Muzzin[13], Gaël Noirot[12], Ghassan T. E. Sarrouh[13], Roberto Abraham[14,15], Yoshihisa Asada[10,16], Gabriel Brammer[17], Vicente Estrada-Carpenter[10], Giordano Felicioni[1], Seiji Fujimoto[14,18], Kartheik Iyer[19], Lamiya Mowla[20] & Victoria Strait[17,21]

Little red dots (LRDs) are a high redshift galaxy population. Despite their high number densities, their nature is still uncertain. Here we present CANUCS-LRD-z8.6, a spectroscopically confirmed little red dot at a spectroscopic redshift of $z_{\rm spec} = 8.6319$, hosting an active galactic nucleus. Its spectrum exhibits broad H$\beta\lambda$4863 Å emission, high-ionization lines (C iv, N iv]), high electron temperature, which are indicative of active galactic nucleus activity, and low metallicity ($Z < 0.1$–$0.2Z_{\odot}$). The inferred black hole mass, $M_{\rm BH} = 1.0^{+0.6}_{-0.4} \times 10^8\ {\rm M}_{\odot}$, poses strong constraints on current black hole formation models and simulations. Additionally, its black hole is over-massive relative to its host, deviating from local $M_{\rm BH} - M_*$ relations, suggesting an early, rapid black hole growth preceding that of its galaxy. CANUCS-LRD-z8.6 may represent an evolutionary link between early massive black holes and the luminous quasars observed at $z = 6$.

LRDs appear as a heterogeneous galaxy population in which both active galactic nuclei (AGN) and star formation can contribute to their observed light. Some LRDs have been classified as AGN hosts based on the detection of broad emission in Balmer lines[1–3], and some show evidence for evolved stellar populations with clear Balmer breaks[4]. Moreover, it has been found that, independent of the specific AGN contribution adopted, the LRDs' black holes (BHs) are significantly overmassive relative to their host galaxies

[1]Faculty of Mathematics and Physics, University of Ljubljana, Ljubljana, Slovenia. [2]IFPU, Institute for Fundamental Physics of the Universe, Trieste, Italy. [3]Scuola Normale Superiore, Pisa, Italy. [4]Astronomy Unit, Department of Physics, University of Trieste, Trieste, Italy. [5]Kavli Institute for Cosmology, University of Cambridge, Cambridge, UK. [6]Cavendish Laboratory—Astrophysics Group, University of Cambridge, Cambridge, UK. [7]NRC Herzberg, Victoria, BC, Canada. [8]European Southern Observatory, Garching, Germany. [9]INAF—Osservatorio Astronomico di Brera, Milano, Italy. [10]Department of Astronomy and Physics and Institute for Computational Astrophysics, Saint Mary's University, Halifax, NS, Canada. [11]Kapteyn Astronomical Institute, University of Groningen, Groningen, The Netherlands. [12]Space Telescope Science Institute, Baltimore, MD, USA. [13]Department of Physics and Astronomy, York University, Toronto, ON, Canada. [14]David A. Dunlap Department of Astronomy and Astrophysics, University of Toronto, Toronto, ON, Canada. [15]Dunlap Institute for Astronomy and Astrophysics, Toronto, ON, Canada. [16]Department of Astronomy, Kyoto University, Kyoto, Kyoto, Japan. [17]Niels Bohr Institute, University of Copenhagen, Copenhagen, Denmark. [18]Department of Astronomy, The University of Texas at Austin, Austin, TX, USA. [19]Columbia Astrophysics Laboratory, Columbia University, New York, NY, USA. [20]Whitin Observatory, Department of Physics and Astronomy, Wellesley College, Wellesley, MA, USA. [21]Cosmic Dawn Center (DAWN), Copenhagen, Denmark. ✉e-mail: roberta.tripodi@inaf.it

https://doi.org/10.1038/s41467-025-65070-x

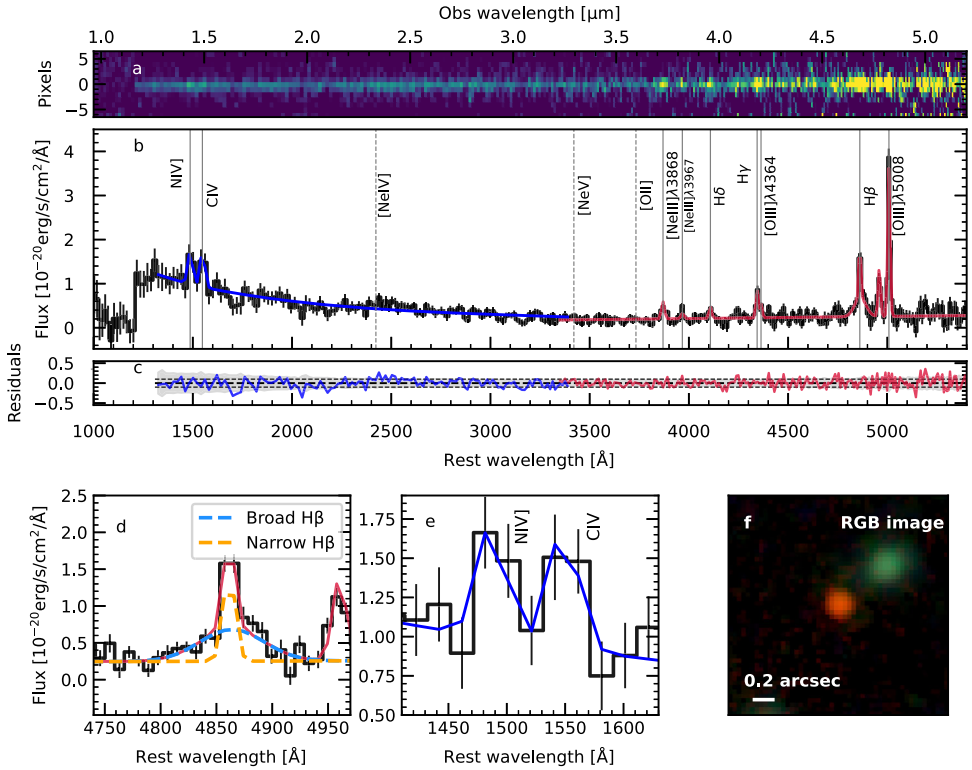

Fig. 1 | NIRSpec PRISM spectrum and RGB image of CANUCS-LRD-z8.6 at $z = 8.6319 \pm 0.0005$. Errorbars are the 1σ noise level. **a** 2D spectrum. **b** The black line represents the measured 1D spectrum. The two independent best-fitting functions for the rest-frame UV and optical part are shown as blue and red solid curves, respectively. Vertical solid (dashed) lines mark detected (non-detected) emission lines, respectively. **c** residuals of the fit of the 1D spectrum. The dashed horizontal lines mark the 0 level and the average ±1σ noise levels derived at λ>2000 Å. The gray shaded area is 1σ rms. **d** Zoom in on the Hβ emission line. The best-fitting spectrum is shown in red, while the narrow and broad Hβ components are shown in yellow and light blue, respectively. **e** zoom-in of the N iv and C iv emission lines. Y-axis has the same label as (**d**). The best-fitting spectrum is shown in blue. **f** RGB image of CANUCS-LRD-z8.6, combining psf-matched imaging using F090W, F200W, and F444W filters. The scale of the image is reported in the lower left corner. The source observed rightward our target is a foreground galaxy at $z_{\rm phot} = 0.49^{+0.05}_{-0.07}$. Source data are provided on Zenodo (see "Data Availability" section).

compared to the local $M_{\rm BH}$–M_* relation[5], and their formation channels remain unclear. Understanding how these massive BHs formed in such compact galaxies as early as redshift $z = 8.6$ remains a key question[1,6].

Here, we present the discovery of the LRD CANUCS-LRD-z8.6 at $z_{\rm spec} = 8.6319 \pm 0.0005$ (object ID: 5112687; RA = 11:49:33.82, DEC = 22:20:59.16), which opens a new pathway to the understanding of this intriguing population of LRDs. Indeed, this source is unique in terms of its BH and host galaxy properties, being the only high-z source to date that shows evidence of broad line emission and high-ionization lines. Throughout the paper, we adopt the ΛCDM cosmology from ref. 7: $H_0 = 67.4$ km s^{-1} Mpc^{-1}, $\Omega_m = 0.315$, and $\Omega_\Lambda = 0.685$. Thus, the angular scale is 4.802 kpc/arcsec at $z = 8.3$.

Results

The target

As part of the Canadian NIRISS Unbiased Cluster Survey (CANUCS) program, JWST/NIRCam and NIRSpec observations of the cluster MACS J1149.5+2223 allowed us to identify and study CANUCS-LRD-z8.6 (Fig. 1). The galaxy was first selected as a high-redshift "double break" galaxy[8], and it also meets the criteria set by ref. 9 on spectral slopes and size to be classified as an LRD. The upper limit derived for the half-light radius of this source is very stringent, $r < 70$ pc (see Section "Observations and data reduction"). Hereafter quantities are corrected for the derived magnification of CANUCS-LRD-z8.6, $\mu = 1.07$ (see Section "Observations and data reduction"), unless otherwise specified.

Evidence of AGN activity

As shown in Fig. 1d, the detection of broad emission in Hβ (S/N = 6), with FWHM$_{\rm H\beta,\,broad} = 4200^{+600}_{-500}$ km s^{-1} (see Section "Continuum and emission line fitting"), indicates the presence of an AGN. The non-detection of broad emission in [O III]λ5008 refutes the scenario of the high gas velocities arising from outflowing material. From locally-calibrated empirical relations[10] using both the broad Hβ luminosity and the L_{5100} Å continuum luminosity, we derive consistent values for the BH mass of $M_{\rm BH} = 1.0^{+0.6}_{-0.4} \times 10^8$ M$_\odot$. This picture is further supported by the detection of high ionization lines of N iv] and C iv (both at S/N = 3; Fig. 1e). These are typical indicators of Type II AGNs[11], and have been seen with JWST in galaxies identified as Type II AGNs[12,13]. For CANUCS-LRD-z8.6, the detection of both N iv] and C iv cannot be explained as arising from star formation [as in ref. 14, see Section C iv, N iv]$\lambda\lambda$1483,1486, Nv, and [Nev]]. Moreover, the combination of very high-velocity broad line gas (>1000 km s^{-1}) and high-ionization narrow emission lines with high photo-ionization energy (about 50–60 eV) constitutes a strong AGN signature[1,15,16]. When compared with other spectroscopically well-studied objects at $z > 7$[1,14,17–23], CANUCS-LRD-z8.6 stands out given that it is one out of the two only sources showing both broad emission in Hβ and the detection of N iv] and C iv, but the other one being at lower z (J1007-AGN at z=7.3;[23]). At the same redshift, the LRD found by ref. 1 has similar BH mass to our target, but no evidences of high-ionization lines and lower stellar mass (see also the discussion in Section "Properties of the host galaxy"). Moreover, the BH mass of CANUCS-LRD-z8.6 is at least one order of magnitude higher than the majority of spectroscopically confirmed AGN LRDs at z ~5–7[9,24], with just three LRDs with comparable BH mass at lower

https://doi.org/10.1038/s41467-025-65070-x

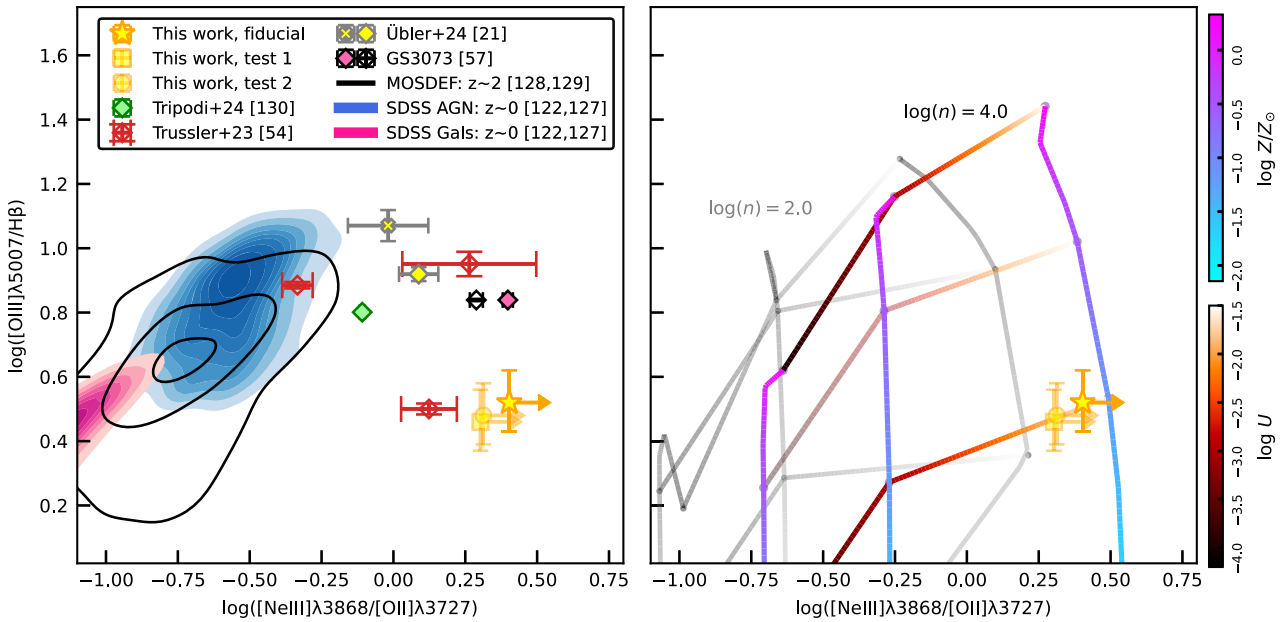

Fig. 2 | [O III]λ5007/Hβ–[Ne III]λ3869/[O II]λ3727 narrow line ratio diagram. The fiducial result for CANUCS-LRD-z8.6 is shown as a yellow star. The lighter yellow square and circle are the results for the line ratios of CANUCS-LRD-z8.6 from Test 1 and Test 2, respectively, derived by adding a broad Hγ component (see text and Supplementary Methods). Line ratios are dust-corrected. The maximum correction for [Ne III]λ3869/([Ne III]λ3869+Hζ+Hη) due to the blend of [Ne III]λ3869, He Iλ3889, Hη and Hζ is ≈ 0.2 dex (see Section "Line blending and contamination correction"). Errorbars represent standard deviation. Left: the [O III]λ5007/Hβ ratio as a function of the [Ne III]λ3869/[O II]λ3727 ratio ("OHNO" diagnostic) for our target and other observations as described in the legend and in Supplementary Methods (Section "Electron temperature and metallicity"). Contours are reported as bars in the legend. Right: overlaid to our results (yellow markers as in the legend of the left panel) for the "OHNO" diagnostic are the AGN photoionization models of ref. 11 at hydrogen densities log n[cm^{-3}] = 2.0 (gray scale grid) and log n[cm^{-3}] = 4.0 (coloured-scale grid). The grid shows the variation of the ionization parameter and metallicity (color scales on the right-hand side of the figure, same limits are adopted for gray scale). To guide the eye, lighter colors represent lower metallicity and higher ionization. Y-axis is the same as the right panel. Source data are provided on Zenodo (see "Data Availability" section).

z ~ 5–7. Notably, compared to the AGN candidate GN-z11 at z = 10.6, which also exhibits N iv] and C iv emission[17,18], CANUCS-LRD-z8.6 hosts a supermassive black hole (SMBH) approximately 100 times more massive than that of GN-z11, despite being just 150 Myr older.

Properties of the host galaxy

As anticipated above, the properties of CANUCS-LRD-z8.6's host galaxy also add interesting details to the picture, specifically in terms of the composition of the gas and the co-evolution between the SMBH and its host. No Lyman-α emission has been detected, and the shape of the spectrum around Lyman-α seems to indicate the presence of a damping wing[25–27]. Since the auroral [O III]λ4364 emission line has been detected with S/N = 4, albeit blended with a stronger Hγ line, we can determine the electron temperature (T_e) and the gas-phase metallicity. We find an extreme [O III]λ4364/[O III]λ5008 ratio (about −1 dex) even after subtracting an additional broad Hγ component: in particular, we assumed the broad Hγ to have the same width of the observed broad Hβ, and the ratio of the peak fluxes of the broad Hγ over broad Hβ to be either equal to case B recombination (Test 1) or equal to the ratio of the fluxes of the narrow components (Test 2). These extreme [O III]λ4364/[O III]λ5008 ratios are found to be suggestive of high densities as in the densest part of the narrow line region of Type I AGNs[28]. Using `pyneb` models, we derive $T_e = 40,000^{+16,000}_{-12,000}$ K, which is 2-4 times higher than in star-forming galaxies[29,30], but consistent with other AGNs[1,31]. Even when considering the maximum Hγ contribution, the electron temperature is at least > 20, 000 K. In particular, similarly to our source, ref. 1 found extreme high electron temperature in an LRD at z = 8.5 also showing broad Hβ emission with FWHM = 3439 km s^{-1}. These features led the authors to identify the LRD as a broad-line AGN, even in the absence of high ionization UV emission/absorption lines (e.g. C IV, N IV], N V). Therefore, such a high electron temperature further supports the presence of an AGN in CANUCS-LRD-z8.6. Moreover, when comparing the [O III]λ4364/Hγ versus [O III]λ5008/[O III]λ4364 line ratio diagram as done in[21,32], our target occupies the region of higher electron temperatures and displays elevated ratios of [O III]λ4364/Hγ compared to local AGNs, similar to the z = 7.15 AGN type I's host galaxy ZS7, identified as a broad-line AGN[21]. There are two non-exclusive possible explanations for the [O II]3727 non-detection. (1) Given the high-ionization inferred for CANUCS-LRD-z8.6, it is likely that [O II]3727 is almost completely ionized and so detected as [O III]λ5008. This hypothesis resonates with the generally lower [O III]λ5008/[O II]3727 ratios found by JWST in galaxies at z > 5 [e.g. refs. 33]. While luminous AGN can show substantial [O II]3727 emission, in general the low-ionization zone in AGNs is associated with high-energy, small cross-section photons, chiefly X-rays [e.g., refs. 34]. However, for LRD AGNs, the X-ray detection is very low[35–37], naturally explaining the lack of [O II] 3727. (2) The other possibility is that of emission dominated by high-density regions[38]; with electron densities above about 10^4 cm^3, capable of collisional suppression of the [O II]3727 emission, but still too low density to equally suppress [O III]λ5008. Finally, a more speculative hypothesis is that [O III]λ5008 may trace a compact, high-surface brightness source, while [O II]3727, if more diffuse, would be below our detection threshold. The stringent upper limit on the [O II]3727 emission line provides strong constraints on the metallicity content of this LRD. Indeed, the 3σ upper limit inferred from the T_e-direct method is low, $Z \lesssim 0.2Z_\odot$ (see Section "Electron temperature and metallicity").

These results are also consistent with those derived from "OHNO" diagnostic, shown in Fig. 2, which relates the [O III]5008/Hβ with [Ne III]λ3869/[O II]3727 to distinguish between the star-forming or AGN nature of galaxies at low- and high-z[39–41]. Also in this case, the observed "OHNO' ratios (yellow star) clearly indicate low metal content ($Z \lesssim 0.1Z_\odot$) and high ionization parameter (log(U) ∼ −1.5) when

https://doi.org/10.1038/s41467-025-65070-x

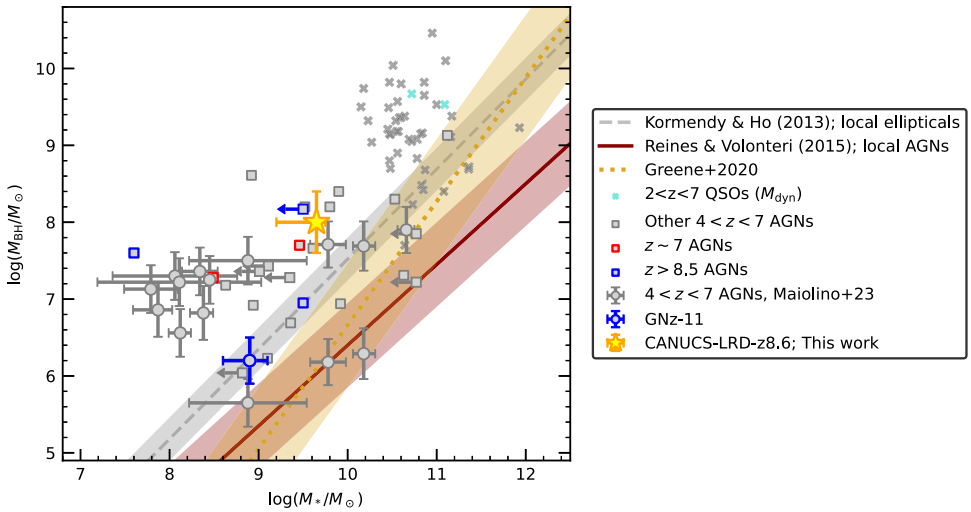

Fig. 3 | Black hole mass versus stellar mass. The results for CANUCS-LRD-z8.6 (yellow star) are compared with $4 < z < 7$ AGNs (gray dots) from ref. 55, a compilation of QSOs at $4 < z < 7$[187], a compilation of AGNs at $4 < z < 7$ (gray squares) discovered by other JWST surveys at high-z[4,36,188–190], AGNs at $z \sim 7$ (red edged squares[21,24]), AGNs at $z > 8.5$ (blue edged squares[1,41,58]), GNz-11 at z=10.6 (blue edged dot,[55]) and with local scaling relations [dashed gray, solid red and dotted yellow lines, respectively from refs. 51,191,192]. Error bars represent standard deviation. Source data are provided on Zenodo (see "Data availability" section).

comparing with photo-ionization models. CANUCS-LRD-z8.6 shares similar metallicity content as the galaxy 04590 at $z = 8.497$ presented in ref. 42 (red square in Fig. 2). 04590 is reported to have a comparable [O III]/Hβ ratio to $z = 0$ dwarf galaxies, given its stellar mass of $\log M_* \sim 8.5 \pm 0.3$. The scenario for our target changes significantly, given that CANUCS-LRD-z8.6 stellar mass is about 1 dex higher than 04590.

Indeed, by performing Spectral Energy distribution (SED) fitting using both photometry and spectroscopy with `Bagpipes`[43,44], including an AGN component, we derive a stellar mass of $M_* = 4.5^{+1.1}_{-2.9} \times 10^9$ M$_\odot$ (errors include possible variation of the SED and dust modeling, see Section "Spectral energy distribution fitting"). As shown in Fig. 3, in terms of stellar mass, CANUCS-LRD-z8.6 is indeed the most massive AGN host at $z > 7$. When comparing both the [O III]/Hβ and [Ne III]λ3869/[O II] ratios as a function of M_*, in the local UNiverse SDSS galaxies exhibit a bimodal distribution[42]. At $\log M_* \lesssim 10$, both line ratios are anti-correlated with stellar mass, forming the so-called "main sequence". In the higher mass regime, AGN activity becomes dominant, leading to elevated line ratios. Due to its large stellar mass, CANUCS-LRD-z8.6 falls within the region of AGN host galaxies, unlike 04590 (see Figure 6 in ref. 42), although it occupies the lower-metallicity end of this distribution. Similarly to other C iv emitters, such as RXCJ2248-ID[14], GHZ2[20], and the $z = 7$ LRD COS-66964[24], CANUCS-LRD-z8.6 is characterized by intense star formation in a very dense and metal-poor environment. Our observations of CANUCS-LRD-z8.6 also reveal nitrogen enrichment alongside the carbon one, which seems to be in tension with the evidence of low metallicity. A possible explanation could be found in the recent discovery of metallicity stratification in AGN hosts[45]. In this picture, the nitrogen and carbon enrichment arise form the broad line region (BLR) surrounding the AGN. This enriched gas in the BLR could be explained by tidal disruption events or accelerated chemical evolution in the very central region. However, given the compact size of the BLR[46], the metallicity enhancement in the BLR does not have a strong impact on the metallicity derived from the overall larger galaxy. Indeed, the low metallicity content found in the galaxy is possibly arising from a recent or ongoing accretion of pristine gas also fueling the star formation, which is high as inferred from the SED fitting ($\log(\mathrm{sSFR}/\mathrm{yr}^{-1}) = [-8.0, -7.9]$). This picture reconciles the observed low metallicity in CANUCS-LRD-z8.6 as arising from the total galaxy with the evidence of N and C enhancements as deriving from the central AGN. It is also worth to highlight that, when considering the most stringent constrain obtained for CANUCS-LRD-z8.6's metallicity ($Z < 0.1 Z_\odot$), CANUCS-LRD-z8.6 is one of the most metal-poor source per given stellar mass observed at these high redshifts [see the mass-metallicity relation shown in ref. 29].

Discussion

We hypothesize a physical model of the CANUCS-LRD-z8.6 system which can account for all of the observations and the derived properties. When modeling its SED including the AGN component, we find that the AGN dominates the UV continuum. Combined with the observed broad Hβ and high-excitation UV lines, this suggests our sight-line to the AGN is not heavily dust-obscured. On the other hand, the fit prefers a lower AGN contribution in the rest-optical regime, instead accounting for the red continuum with more dust obscuration of the stellar component. Given the very compact size of the source and the significant SFR inferred from the modeling (about 50 M$_\odot$ yr^{-1}), it is reasonable to infer that the bulk of the stellar light is embedded in stellar birth clouds, leading to high obscuration. Ref. 47 shows that even small amounts of dust can cause significant obscuration in LRDs given their compactness. Altogether, this points to a highly compact system undergoing an episode of star formation with a high dust covering fraction in which a highly energetic AGN has cleared a sight-line in our direction[48–50]. This perhaps points toward CANUCS-LRD-z8.6 being a more evolved system than some other observed LRDs that exhibit less massive BHs and host galaxies, on its way to becoming a system resembling the brightest quasars at $z = 6$ rather than the lower luminosity AGNs discovered by JWST in this redshift range (see also Section "Comparison with simulations and semi-analytical models"). Figure 4 shows a visual representation of this physical configuration.

LRDs' BHs are found to be significantly overmassive relative to their host galaxies compared to the local $M_{BH} - M_*$ relation[5]. Given the SED-inferred M_*, it is possible to place CANUCS-LRD-z8.6 on the M_{BH}–M_* plane. As presented in Fig. 3, CANUCS-LRD-z8.6 stands above the $M_{BH} - M_*$ local relations (in particular the one for local AGNs, in red;[51]), indicating faster evolution of the BH compared to its host galaxy. This is possibly the result of the BH experiencing fast growth and suppressing star formation via efficient feedback, a scenario that is also supported by recent simulations[52] and observations of quiescent

https://doi.org/10.1038/s41467-025-65070-x

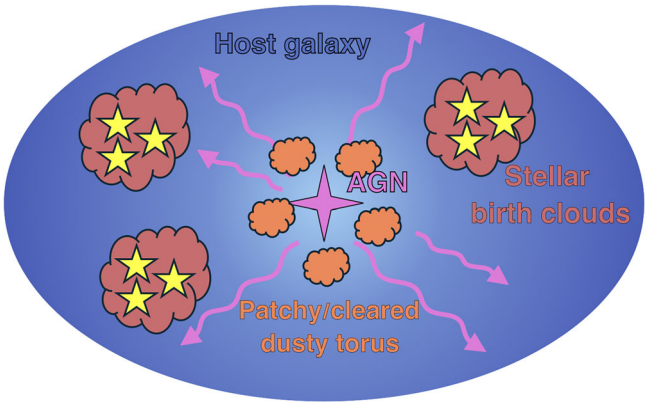

Fig. 4 | Simple visual representation for our hypothesized physical configuration of CANUCS-LRD-z8.6. Components include a UV-bright AGN with either a patchy dusty torus or a sight-line cleared by feedback. Stars are obscured by a high dust covering fraction, likely due to a combination of the current episode of star formation and the compact size. Source data are provided on Zenodo (see "Data availability" section).

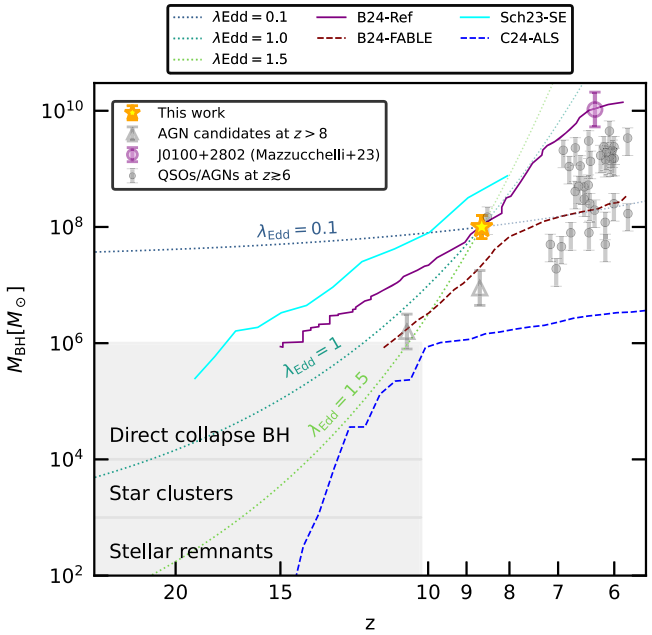

Fig. 5 | Black hole mass accretion history. The growth history of CANUCS-LRD-z8.6 assuming a constant accretion rate corresponding to the observed luminosity ($\lambda_{Edd} = 0.1$), Eddington capped accretion ($\lambda_{Edd} = 1$), and super-Eddington accretion ($\lambda_{Edd} = 1.5$), as blue, teal and light green dotted lines, respectively. Solid purple and dashed red lines are simulations[72], dashed blue[64] and solid cyan[69] lines are semi-analytical models with different prescriptions, as detailed in Supplementary Methods, that can (cannot) reproduce the BH mass of CANUCS-LRD-z8.6. We show for comparison only QSOs and AGNs having BH masses derived from broad lines (as a purple dot[15], and as gray dots[1,21,24,36,41,55,187]), and two AGN candidates at $z > 6$ [as gray triangles[18,41]]. In particular, the source next to our target is the AGN LRD discovered by ref. 1, showing broad Hβ emission but no high-ionization emission lines. Error bars represent standard deviation. Source data are provided on Zenodo (see "Data availability" section).

over-massive black holes[53]. We caution here that these observations may be affected by the combined effects of selection biases (i.e., finite detection limit and limited survey area) and uncertainties in the M_{BH} and M_* estimates[54]. Furthermore, it has been found that outliers from the local M_{BH}–M_* are instead consistent with the local relation M_{BH}–σ, where σ is the stellar velocity dispersion[53,55]. This suggests that M_{BH}–σ is a more fundamental and universal relation than M_{BH}–M_*, and should be preferred when σ measurements are available. This is not the case for CANUCS-LRD-z8.6, and we therefore consider the estimate of M_*, as inferred from the SED fitting.

We are witnessing the growth of an SMBH of 10^8 $M_\odot$ in a very compact and massive galaxy ($M_* \simeq 5 \times 10^9$ $M_\odot$ in $r < 70$ pc), unlike any other sources at the same redshift. The SMBH in CANUCS-LRD-z8.6 has a comparable mass to that of GS-9209 at $z \sim 4.7$, with the critical difference that GS-9209 is quenched, having halted star formation by $z \sim 7$[56]. Additionally, the stellar mass of CANUCS-LRD-z8.6 appears to be approaching that of the massive post-starburst galaxy RUBIES-UDS-QG-z7 ($M_* \sim 1.7 \times 10^{10}$ $M_\odot$,[57]), which is already quiescent at $z \sim 7$. These observations suggest that feedback from SMBHs as massive as CANUCS-LRD-z8.6 could play a pivotal role in quenching star formation in galaxies by $z \sim 7$.

The high BH mass of CANUCS-LRD-z8.6 at $z = 8.6$ imposes stringent constraints on the formation pathways of SMBHs, challenging standard models and simulations. When examining potential growth trajectories under constant accretion rates (dotted lines in Fig. 5), the mass of CANUCS-LRD-z8.6's BH suggests an origin in massive seed mechanisms[58,59], accreting close to the Eddington limit, and/or in PopIII star remnants [e.g., refs. 60–65], accreting at super-Eddington rates. While lower-mass seeds are easier to account for, sustaining a constant or super-Eddington accretion rate over the BH's history has been largely ruled out by numerous studies [e.g., refs. 66,67]. Notably, if the derived accretion rate of CANUCS-LRD-z8.6's SMBH at z=8.6 ($\lambda_{Edd} = 0.1$, blue dotted line) remained constant over time, it would not be sufficient for the BH to reach the observed mass. We refer to Supplementary Methods for a more exhaustive comparison among semi-analytical models (SAMs) and numerical simulations with different prescriptions, and we summarize here our main findings. In SAMs, Super-Eddington accretion results to be essential to reproduce the black hole mass of CANUCS-LRD-z8.6 at its redshift. The CAT model[68], which includes both light and heavy seeds, showcases multiple tracks that successfully assemble $10^8 M_\odot$ at $z = 8.6$[69] (the most massive one is shown in Fig. 5 with a cyan solid line). These models also predict BHs over-massive with respect to their host galaxies as compared to the local relation, as a result of short bursts of Super-Eddington accretion[70]. Interestingly, the stellar masses predicted by their models at $z \sim 9$ are consistent with the low-mass end of the estimated stellar mass for CANUCS-LRD-z8.6. Most numerical simulations employing standard prescriptions cannot replicate CANUCS-LRD-z8.6's BH mass, since AGN feedback prevents early BH growth. In particular, the original recipe of the Feedback Acting on Baryons in Large-scale Environments (FABLE) zoom-in simulations falls short by one order of magnitude (purple dotted track in Fig. 5). FABLE suite of cosmological hydrodynamical simulations are based upon the framework of the successful Illustris project but improve upon the agreement with observations on scales larger than galaxies[71]. However, modifications promoting earlier BH growth to form BHs of $M_{BH} = 10^{10}$ $M_\odot$ at $z \sim 6$[72], such as QSO J0100+2802[15], allow to explain the existence of CANUCS-LRD-z8.6 (purple solid track in Fig. 5; see Section "Comparison with simulations and semi-analytical models"). As such, CANUCS-LRD-z8.6 is a possible progenitor for QSOs like J0100+2802, challenging standard theoretical models. The discovery of CANUCS-LRD-z8.6, featuring one of the highest BH masses and the highest stellar mass at $z > 8$, provides essential constraints for simulations and theoretical models. Current models need further improvements in the description of BH-galaxy (co)-evolution through more refined prescriptions in terms of black hole seeding, star formation physics, AGN feedback and BH accretion modeling, in order to provide a coherent framework able to reproduce at the same time QSOs at $z < 7$, the new population of over-massive AGNs at $4 < z < 7$, and the extreme SMBHs at $z > 8$, such as CANUCS-LRD-z8.6 and UNCOVER 20466[1]. As such, CANUCS-LRD-z8.6 represents a fundamental piece to complete this puzzle.

METHODS

Observations and data reduction

We utilize data from the CANUCS NIRISS GTO Program #1208[73], which targets five strong-lensing cluster (CLU) fields: Abell 370, MACS J0416.1-2403, MACS J0417.5-1154, MACS J1149.5+2223 (hereafter MACS1149, z = 0.543), and MACS J1423.8+2404[74,75]. Because NIRCam and NIRISS operate in parallel, each cluster field includes both a NIRCam and a NIRISS flanking field. Our source of interest is located in the MACS1149 cluster field, which was observed with the following NIRCam filters: F090W, F115W, F150W, F200W, F277W, F356W, F410M, and F444W, each with an exposure time of 6.4 ks. To complement these observations, we also incorporate archival HST imaging from the HFF program[76]. The CANUCS image reduction and photometry procedures are described in detail in refs. 77–80, while the methodology for point-spread function (PSF) measurement and homogenization is presented in ref. 81. Cluster galaxies and intra-cluster light (ICL) are modeled and subtracted to prevent contamination of the photometry following[82]. Briefly, the NIRCam data are processed using a modified version of the Detector1Pipeline (calwebb_detector1) from the official STScI pipeline, together with the jwst_0916.pmap JWST Operational Pipeline (CRDS_CTX). The reduction steps include astrometric alignment of the JWST/NIRCam exposures to the HST/ACS reference frame, sky subtraction, and drizzling to a common pixel scale of 0.04″ using version 1.6.0 of the Grism Redshift and Line Analysis software for space-based slitless spectroscopy (Grizli;[83]). PSFs are empirically derived by median stacking bright, isolated, non-saturated stars, following the methodology of ref. 81, and all images are subsequently degraded to match the F444W resolution for photometry. Source detection and photometric measurements are carried out using the Photutils package[84] on a χ_{mean} detection image created by combining all available NIRCam images.

First selected as a high-z double break galaxy[8], our target is classified as an LRD following the criteria on UV and optical slopes and compactness given by ref. 9.

The CANUCS program also includes NIRSpec low-resolution prism multi-object spectroscopic follow-up using the Micro-Shutter Assembly (MSA[85]). Details of the NIRSpec processing are given in ref. 8. NIRSpec data have been reduced using the JWST pipeline for stage 1 corrections and then the msaexp[86] package to create wavelength-calibrated, background-subtracted 2D spectra. A 1D spectrum is extracted from the 2D using an optimal extraction based on the source spatial profile. The redshift (and its uncertainty) of CANUCS-LRD-z8.6, $z = 8.6319 \pm 0.0005$, was determined by performing a non-linear least-squares fit simultaneously to the Hβ, [O III]λ4960 and [O III]λ5008 emission lines. Each line was modeled with a single Gaussian and the ratio of [O III]λ4960 to [O III]λ5008 was fixed by atomic physics.

The MACS1149 cluster strong lensing model was derived using Lenstool software[87] and the catalog of 91 multiple images with spectroscopic redshifts, derived from CANUCS data[77]. As the distance of the LRD from the cluster centre is large (approximately 3 arcmin), the contribution from the cluster lens model alone is small ($\mu = 1.060 \pm 0.003$). However, the LRD is only 0.54 arcsec away from a foreground galaxy 5112688 at photometric redshift $z_{\rm phot} = 0.49^{+0.05}_{-0.07}$ and stellar mass $\log(M_*/M_\odot) = 8.0 \pm 0.1$ (derived with DenseBasis,[88]). We evaluated the combined magnification in two ways. First, we constructed a Lenstool model containing the cluster model and the foreground galaxy at cluster redshift $z = 0.54$ (we verified that using a slightly lower photometric redshift for the galaxy did not affect the results). We modeled the foreground galaxy as a singular isothermal sphere, where the integrated velocity dispersion ($\sigma = 40^{+4}_{-2}$ km s^{-1}) was derived from log M_* and the stellar mass Tully-Fisher relation[89]. We find that the combined model still yields only a low magnification of $\mu = 1.13^{+0.02}_{-0.01}$. Alternatively, we computed the magnification by modeling the galaxy as a dual pseudo-isothermal ellipse[90], following the scaling relations of other cluster members and by using its F160W magnitude of 25.28 ± 0.03 (we verified that the magnitude uncertainty has a negligible impact on magnification). The scaling relations for parameters were constrained with Lenstool in the inner cluster regions. This method gives a more modest total magnification of $\mu = 1.066^{+0.004}_{-0.002}$. We take the latter value as our best magnification estimate $\mu = 1.07^{+0.08}_{-0.01}$. Considering that the uncertainty derived from different estimates is small, we correct masses, luminosities, and sizes presented in this work for CANUCS-LRD-z8.6 for a constant μ = 1.07.

Supplementary Fig. 1 shows the photometry of our target in 10 bands. We fit CANUCS-LRD-z8.6 with Galfit[91] and confirm that it is spatially unresolved in all filters (see Supplementary Fig. 1). From Galfit modeling, the object is consistent with a point source in all observed NIRCam filters. We perform a more refined fit accounting for the effect of gravitational lensing with Lenstruction[92–94] to place a more stringent limit on the physical size. Lenstruction performs forward modeling accounting for lensing and the instrumental point spread function. We use lensing maps from the main cluster model, which yields a conservative magnification estimate of $\mu = 1.056$, and we choose a clear single star as PSF reference. We use 20 mas image in the F150W filter as this filter comes with the smallest PSF size while still retaining enough flux. The half-light radius of the object results to be smaller than <0.015 arcsec with 95% confidence. This corresponds to an upper limit on the physical half-light radius of 70 pc.

Continuum and emission line fitting

The emission lines are fitted to the 1D spectrum of CANUCS-LRD-z8.6 using single or multiple Gaussian components (see below for details). LRDs often have a characteristic continuum shape, with a blue colour in the rest-frame UV and red in the rest-frame optical. This is why we split the continuum emission of CANUCS-LRD-z8.6 into two parts modeled by two independent power laws. In particular, we divide the spectrum in two parts visually setting $\lambda_{\rm rest,sep} = 3400$ Å, wavelength at which the continuum slope changes sign. Any choice for $\lambda_{\rm rest,sep}$ in the range 3300–3600 Å led to perfectly consistent results. Although our spectrum does not display a prominent break at this location, we note that the wavelength at which our spectrum changes slope is similar to that of breaks observed in other LRDs[4,36] which have been interpreted as Balmer breaks. We discuss a possible physical interpretation of the spectral shape in Section "Spectral energy distribution fitting". We fit the two parts (UV and optical) of the spectrum separately (see Fig. 1). The spectrum is fitted, accounting for the well-known variation of prism resolution with wavelength (see below).

The continuum shows the typical V-shape, having $\beta_{\rm opt} = 0.96 \pm 0.24$ in the optical and $\beta_{\rm UV} = -1.7 \pm 0.1$ in the UV regime, which is in line with the spectral shape of other photometric and spectroscopically confirmed LRDs[9,24]. No Lyman-α emission has been detected, and the shape of the spectrum around Lyman-α seems to indicate the presence of a damping wing[25–27]. The analysis of Lyman-α damping wing is beyond the scope of this paper. Therefore, we exclude the part of the spectrum with $\lambda_{\rm rest} < 1320$ Å, avoiding any contamination from a possible damping wing given the damping wing's size commonly found in the literature (about 2000–3000 km s^{-1}, see e.g., refs. 95,96). Above $\lambda_{\rm rest}$ = 1320 Å, any detected emission line has been modeled with a single or multiple Gaussian components in case of line blending or broad emission.

The [OIII]$\lambda\lambda$4959,5007 doublet is modeled by fixing the ratio between the peak fluxes ($\rm peak_{[O\,III]\lambda4959}/peak_{[O\,III]\lambda5007} = 0.335$) and the rest-frame wavelength separation ($\Delta\lambda = 47.94$ Å) of the two lines, while assuming the same FWHM for both components. Similarly, the [Ne III] λ3869 and [Ne III]λ3967 doublet is fitted by adopting a fixed flux ratio of 0.301 between the latter and the former, and a rest-frame wavelength separation of 98.73 Å, again using a common FWHM for both lines. These constraints reduce the number of free parameters for each of the [O III] and [Ne III]λ3869 doublets to three. Given the prism

resolution, the [Ne III]λ3869 line remains blended with Hζ, Hη, and He Iλ3889 (see the following section).

Apart from these two doublets, there are six other emission lines detected: N iv], C iv, Hδ, Hγ, [O III]λ4368, and Hβ. Each emission line is fitted with a single Gaussian, with the only exception of Hβ, which shows signatures of a broad emission (see Supplementary Table 1). When trying to fit Hβ with one single Gaussian component, the resulting $\sigma_{H}\beta$ is greater than $\sigma_{[O\ III]\lambda5008}$ by more than 7%, which is the expected difference due to the poorer spectral resolution at $\lambda_{H}\beta$. Even though Fe emission can affect the Hβ region, we did not consider Fe features impactful for our analysis for two main reasons: (1) low-luminosity AGNs, including LRD AGNs, do not show evidences of FeII bump or Fe enhancement neither individually nor in stack[97], while they are seen in QSOs possibly metal rich, which is definitely not the case of our target; (2) the low spectral resolution of the prism prevents us to disentangle the possible Fe feature from both the broad and narrow Hβ components. Thus, the Hβ emission line is modeled with two Gaussians accounting for both the narrow and broad components.

For the UV part of the spectrum, we have 8 free parameters in total (i.e., peak flux, peak wavelength, and FWHM for N iv and same for C iv, power-law exponent and normalization for their underlying continuum), while for the optical part we have 24 free parameters: i.e., peak flux, peak wavelength, and FWHM for [Ne III]λ3869, [O II], Hδ, Hγ, Hβ_{narrow}, [O III]λ5007; peak flux and FWHM for Hβ_{broad}; peak flux and wavelength for [O III]λ4364, given that we fixed $FWHM_{[O\ III]\lambda4364}$ = $FWHM_{[O\ III]5008}$; power-law exponent and normalization for their underlying continuum. We explore the parameter space for each part of the spectrum using a Markov chain Monte Carlo (MCMC) algorithm implemented in the `EMCEE` package[98], assuming uniform priors for the fitting parameters, considering 5 walkers per parameter and 2000 trials (the typical burn-in phase is about 200 trials). Priors on the FWHM are tight, depending on the resolution of the prism, with the exception of the $FWHM_{broadH\beta}$. More precisely, the prior on the FWHM of the narrow component of every fitted emission line is set to be $FWHM^{prior}_{narrowline} \in [1, 2]$ spectral resolution elements. The size of the spectral resolution element at the peak wavelength of each fitted line is derived considering the well-known variation of the prism resolution with wavelength[99].

We compute the integrated fluxes by integrating the best-fitting functions for each emission line. In Supplementary Table 1, we report the fluxes and widths of the fitted emission lines. Unless otherwise stated, we report the median value of the posterior, and 1σ error bars are the 16th and 84th percentiles. Upper or lower limits are given at 3σ.

Hγ and [O III]λ4364

Given the resolution of the prism, Hγ is blended with [O III]λ4364; nonetheless, a clear peak at the nominal [O III]λ4364 wavelength is observed (see Supplementary Fig. 2). Therefore, we fitted the blend using two Gaussian components and the results are shown in the Supplementary Table 1 (see Fiducial). Since we detected significant broad Hβ emission, a broad Hγ component could be present along with the narrow Hγ and [O III]λ4364 emission lines. We try to evaluate its impact on our results, considering the detection of the broad Hβ emission. Hence, we re-fitted the spectrum, adding an additional Gaussian component to the Hγ-[O III]λ4364 blend with $FWHM_{H\gamma} = FWHM_{H\beta}$, $\lambda^{peak}_{H\gamma_{broad}} = \lambda^{peak}_{H\gamma_{narrow}}$ and the $F^{peak}_{H\gamma_{broad}}/F^{peak}_{H\beta_{broad}}$ ratio corresponding to Case B recombination (see Test 1 in Supplementary Table 1). Alternatively, we also fitted the broad H_γ component considering $F^{peak}_{H\gamma_{narrow}}/F^{peak}_{H\gamma_{broad}} = F^{peak}_{H\beta_{narrow}}/F^{peak}_{H\beta_{broad}}$ (see Test 2 in Supplementary Table 1). The spectral resolution and sensitivity of our data do not allow us to be conclusive regarding the presence of a broad Hγ component, as shown in Supplementary Fig. 2. Even though the broad Hγ over-predicts the data at $\lambda_{rest} \sim 4300$ Å, this is within $1-2\sigma$, leading to good residuals. Based on the reduced χ^2 criteria, the preferred solution is the one without the broad Hγ component (Fiducial), however the other two tests give still reasonably good fits. Therefore, hereafter, we will present primarily the results of our Fiducial fit, and we will discuss the uncertainties introduced by the possible broad Hγ component using the results from Tests 1 and 2.

Dust correction

In order to estimate the electron temperature, T_e, and the gas-phase metallicity (hereafter metallicity), O/H, line fluxes need to be corrected for dust reddening. We derive the nebular reddening, $E(B-V)_{neb}$, using the observed ratio of H Balmer lines, Hβ and Hγ, assuming the Calzetti attenuation law[100]. Indeed, the attenuation curve of high-z galaxies is found to be consistent with the Calzetti law. Regarding the observed Hγ/Hβ ratio, we consider the three cases described in the previous section, depending on whether and how a broad Hγ component is included. To derive the reddening, we could have also used Hδ but, given the low S/N of this line (lower than for Hγ), we cannot evaluate the possible uncertainties introduced by the presence of a broad component. The intrinsic Balmer ratios are computed using `pyneb`[101] assuming $T_e = 10^4$ K, and $n_e = 10^3$ cm^{-3}; results remain in agreement within error bars even if considering $T_e = 2\times10^4$ K, and $n_e = 10^4$ cm^{-3}. The derived nebular reddening and dust attenuation are reported in Supplementary Table 2. We note that the negative value found for our Fiducial model suggests the presence of a broad Hγ component, which adjusts the dust attenuation to a more reasonable value (see also Section "Spectral energy distribution fitting for a comparison with the stellar A_V from SED fitting"). Emission line ratios are then computed using the reddening-corrected fluxes (see Supplementary Table 2). By definition, due to the proximity of the involved lines, [O III]λ5008/Hβ, [Ne III]λ3869/[O II]3727, and C iv/N iv] show almost no dependence on the reddening correction. These are the line ratios of interest for our study. [O II]3727/Hβ shows a variation of about 0.3 dex comparing the Fiducial with Test 1/2 models (when considering a broad Hγ component).

Line blending and contamination correction

When measuring [Ne III]λ3869, we also account for the flux contributions from Hη, Hζ (λ = 3890.17 Å), and He Iλ3889, all of which are blended with [Ne III]λ3869 at the spectral resolution of the prism. We define the total blended flux as $[NeIII]_{blend}$ = [Ne III]λ3869 + Hζ + He Iλ3889 + Hη. To estimate the contamination from these additional lines, we proceed as follows. For Hζ and Hη, we compute the dust-corrected flux ratio H$\delta/[NeIII]_{blend}$ from the fiducial fit (see Supplementary Table 2), obtaining a value of $0.63^{+0.28}_{-0.20}$. Assuming the theoretical Balmer line ratios from Case B recombination with T_e = 20,000 K and $n_e = 10^4$ cm^{-3}[102], this implies that H$\eta/[Ne\ III]_{blend} < 0.18$ and H$\zeta/[Ne\ III]_{blend} < 0.25$. For He I$\lambda$3889, it is not possible to estimate the contamination reliably because the He I λ5877 line, required for this calculation, is undetected in our data. Thus, we can only constrain the combined contribution of the Balmer lines, finding (Hζ + Hη)$/[NeIII]_{blend} < 0.43$, which in turn implies [Ne III] λ3869$/[NeIII]_{blend} > 0.57$. This represents an upper limit on the contamination, as the effect of He Iλ3889 is not included. Furthermore, using the dust-corrected fluxes derived from either Test 1 or Test 2 yields H$\delta/[Ne\ III]_{blend} = 0.50 \pm 0.20$ and 0.55 ± 0.20, corresponding to [Ne III]λ3869$/[Ne\ III]_{blend} > 0.66$ and >0.63, respectively. Given these uncertainties, we do not apply a contamination correction to [Ne III] λ3869. However, for the fiducial case, we report the magnitude of the estimated contamination in the relevant figures.

Electron temperature and metallicity

We detect the auroral [O III]λ4364 line, which can be used together with the [O III]λ5008 to derive the electron temperature and gas-phase metallicity[103–105]. Indeed, the electron temperature, T_e([OIII]), of the high-ionization O^{2+} zone of the nebula is computed from the dust-corrected [O III]λ4364/[O III]λ5008 ratio (hereafter RO3). In each of the

three cases discussed before, we find a high RO3, possibly indicating the presence of an AGN, a powerful ionizing source. Indeed, in Supplementary Fig. 3 we compare the observed value for RO3 with models from `pyneb`. For the fiducial dust-corrected RO3, $T_e([\mathrm{OIII}]) = 4.0^{+1.6}_{-1.2} \times 10^4$ K, higher than the temperature usually found in normal star-forming galaxies ($T_e([\mathrm{OIII}])$ ~1–2 × 10^4 K)[29,106]. Even when considering the presence of the broad Hγ component, $T_e([\mathrm{OIII}])$ is high within the uncertainty, at least $>2 \times 10^4$ K. Evidently from Supplementary Fig. 3, our result is insensitive to the electron density within a range of $n_e = 10^2$–10^4 cm^{-3}. Using the models of ref. 107, we obtain a consistent result, having $T_e([\mathrm{OIII}]) = 3.9^{+1.6}_{-1.0} \times 10^4$ K. Other extreme RO3 have been found in other galaxies at same redshift[1,108,109], at $z \sim 4$[110], and are also found in low-z Seyfert galaxies[31,111,112]. Moreover, such a high ratio of [O III]λ4364/Hγ as ours ($\log([\mathrm{O\,III}]\lambda4364/\mathrm{H}\gamma) \sim -0.3$) is observed in AGN[113,114]. This can be further seen by comparing nearby AGN and star-forming galaxies from SDSS[115,116] in the[O III]λ4364/Hγ versus [O III]λ5008/[O III]λ4364 line ratio diagram, as done in ref. 21 for ZS7. In this diagram, local star-forming galaxies and AGN separate into two parallel sequences, with AGN occupying a region of higher electron temperatures and having elevated ratios of [O III]λ4364/Hγ. Indeed, our target lies at the extreme end of the AGN population, the farthest from the star-forming galaxies.

We aim to derive a first-order estimate of the metallicity of our source from the total oxygen abundance $\mathrm{O/H} = \mathrm{O^{2+}/H^+} + \mathrm{O^+/H^+}$. To compute $\mathrm{O^+/H^+}$, $T_e([\mathrm{OII}])$ is required. However, none of the [O II] transitions ([O II]3727, [O II]λλ7322,7332) is or can be detected in the spectra. Therefore, we use the relation of ref. 117:

$$T_e([\mathrm{O\,II}]) = 0.7 \times T_e([\mathrm{OIII}]) + 3000\ \mathrm{K}, \quad (1)$$

where T_e is the electron temperature of the species in parentheses. For our fiducial case, $T_e([\mathrm{O\,II}]) = 3.1 \times 10^4$ K. Ionic and total oxygen abundances are computed using `pyneb`, assuming that all O is in either the $\mathrm{O^{2+}}$ or $\mathrm{O^+}$ states inside HII regions. Indeed, $\mathrm{O^{3+}}$ may be neglected considering that it is <5% of the total O even in very high-ionization systems[118,119] and it is negligible given the uncertainty of our computations. The $\mathrm{O^{2+}}/H^+$ ratio is derived from the dust-corrected [O III]5008/Hβ, the $\mathrm{O^+/H^+}$ ratio from the dust-corrected [O II]3727/Hβ upper limit, and we assume the $T_e([\mathrm{OIII}])$, $T_e([\mathrm{O\,II}])$ derived above for the fiducial case. Given that the upper limit on [O II]3727/Hβ ratio and that the highest allowed electron temperature in Pyneb models is $T_e = 3 \times 10^4$ K, we can derive an upper limit on the metallicity. Indeed, O/H ratios decrease at fixed line ratios and increasing electron temperature. The inferred metallicity of our source is $12 + \log(\mathrm{O/H}) < 7.9$ or $\log(Z/Z_\odot) < -0.7$. The upper limit becomes more stringent if considering the presence of the broad Hγ component (either Test 1 or 2), having $12 + \log(\mathrm{O/H}) < 6.9$ or $\log(Z/Z_\odot) < -1.8$. As a word of caution, we mention that the possible presence of very high-density regions ($\log(n_e) > > 4$) have an impact on the observed flux of the [O III]λ5008 line due to the collisional de-excitation of the lower level [O III]λ5008 bearing transition[38,45]. However, the available data prevent us from quantifying this effect since the density distribution cannot be derived.

Additional evidence that CANUCS-LRD-z8.6 is metal-poor comes from the comparison of its position on the "OHNO" diagnostic diagram, which relates the line ratios [O III]5008/Hβ and [Ne III]λ3869/[O II]3727, with photoionization models (see Fig. 2). This diagnostic has been widely used to distinguish between star-forming galaxies and AGN, both at low and high redshift[39–41]. In the left panel of Fig. 2, we compare our measurements with several reference samples: $z \sim 0$ SDSS AGNs (blue colormap with contours) and galaxies (pink colormap with contours)[116,120]; $z \sim 2$ MOSDEF galaxies and AGNs (black contours)[121,122]; three systems at $z > 6$, namely SMACS 06355, 10612, and 04590 (red diamonds;[42], where the left-most diamond corresponds to SMACS 06355, the type-II AGN identified by ref. 114); the type-I AGN host GS 3073 at $z = 5.55$ (filled pink and hollow diamonds, the latter representing the [Ne III]λ3869 flux estimated under the Case B assumption modulated by the median dust attenuation;[45]); the type-I AGN host ZS7 at $z = 7.15$ (yellow cross and diamond, depending on whether the line fluxes are derived from the BLR location or from the [O III] centroid, respectively;[21]); and a stack of AGNs from the JWST Advanced Deep Extragalactic Survey (JADES) in the range $4 < z < 11$ (green diamond;[123]). In the right panel of Fig. 2, we overlay AGN photoionization models from ref. 11 at hydrogen densities of $\log n[\mathrm{cm^{-3}}] = 2.0$ (grayscale) and $\log n[\mathrm{cm^{-3}}] = 4.0$ (colored scale). The observed "OHNO" ratios for CANUCS-LRD-z8.6 indicate a low metallicity, pointing toward $\log(Z/Z_\odot) < -1.0$. Moreover, our stringent lower limit on [Ne III]λ3869/[O II]3727 implies a highly ionized gas, corresponding to an ionization parameter of $\log U \sim -1.5$, consistent with values reported for other AGN candidates at $z > 8$[1,41].

As an alternative approach, we also estimate the gas-phase metallicity directly from the fiducial dust-corrected [O III]5008/Hβ ratio using the empirical calibration presented in refs. 106,124,125, under the assumption that the narrow emission lines are dominated by star formation. This yields metallicities of $12 + \log(\mathrm{O}/H) = 7.08^{+0.14}_{-0.12}$ ($Z \sim 0.02 Z_\odot$), $12 + \log(\mathrm{O}/H) = 7.40^{+0.13}_{-0.11}$ ($Z \sim 0.05 Z_\odot$), and $12 + \log(\mathrm{O}/H) = 7.28^{+0.15}_{-0.12}$ ($Z \sim 0.04 Z_\odot$), respectively. These values are fully consistent with the results from the "OHNO" diagnostic, which indicate $Z \ll 0.1 Z_\odot$.

C iv, N iv]λλ1483,1486, N V, and [Ne v]

High-ionization lines requiring photoionization energy >50–60 eV, such as N iv], N V, and [Ne v] are signatures of the presence of an AGN. Even though C iv is also usually associated with the presence of a central AGN[15,18], it is not an unambiguous tracer of an AGN in the absence of other signatures (e.g., N iv, broad emission), since it has also been detected in some low-mass low-Z galaxies at high-z. We have clear evidence of N iv] and C iv emission, while both N V and [Ne v] remain undetected, as well as [C III]. We note, however, that the resolution of the prism does not allow us to assess the presence of N V since it is blended with the Lyα and its damping wing. In many AGNs some of these emission lines are either very weak or undetected if the S/N is not high enough[126–128]. For instance, in the type 1.8 AGN GS-3073 at $z = 5.5$[129–131], the N V is five times weaker than N iv], which would be totally undetected in our spectrum. Similarly, N V is undetected in GNz-11[18] and in other type 1 quasars[132], while N iv] is strong. As discussed in refs. 18,132, [Ne v]/[Ne III]λ3869 can be quite low in AGNs, down to 10^{-2}–10^{-4}. The simultaneous detection of both C iv and N iv] in galaxies at $z \sim 7$ has been attributed to ionization by dense clusters of massive stars formed during an intense burst of star formation[14]. This interpretation is supported by high observed specific star formation rates (sSFR > 300 − 1000 Gyr^{-1}) and large Hβ equivalent widths (EW > 400–600 Å). However, for CANUCS-LRD-z8.6, this scenario is unlikely due to its very low inferred sSFR (sSFR < 10 Gyr^{-1}; see Section "Spectral energy distribution fitting" and Figure 18 in ref. 14), indicating that sources other than massive stars are needed to account for its strong ionization.

Given the uncertainties on the dust correction given by the possible presence of a broad Hγ component and the absence of the [O III]λ1666 emission line in the UV, we will just discuss the C iv/N iv] ratio, which is reddening insensitive, leaving aside the discussion about the C/O or N/O ratios, which would be severely affected by the uncertainties in the dust correction. Assuming that all the nitrogen is in $\mathrm{N^{3+}}$, emitted in N iv], and all the carbon in $\mathrm{C^{3+}}$, emitted in C iv, we obtain a low C iv/N iv] ratio, having dust corrected $\log(\mathrm{CIV/NIV}) = 0.07 \pm 0.3$. Assuming a temperature of 40,000 K as derived from the [O III]λ4364/[O III]λ5008 ratio and a density of $n_e = 10^3$ cm^{-3}, we infer a carbon-over-nitrogen abundance of $\log(\mathrm{C/N}) = -0.75^{+0.05}_{-0.04}$. Such low C/N abundance ratio is similar to what was reported for some nitrogen-enriched galaxies observed at high redshift[133], and aligns with

abundance patterns measured for dwarf stars in local globular clusters[134], possibly suggesting that material-enriched through the CNO cycle has been effectively ejected via powerful stellar winds from the outermost layers of massive stars[135–137].

Black hole mass and bolometric luminosity of the AGN

Robust estimates of BH masses usually come from reverberation mapping studies, which unfortunately are not feasible at high-z. Therefore, the so-called single-epoch virial mass estimate of M_{BH} is often used[15,55], assuming that virial relations are still valid at high-z and considering the continuum or line luminosity and the FWHM of the broad emission lines. For this work, we use the empirically derived relation:

$$\frac{M_{BH}}{M_\odot} = \alpha \left(\frac{L_\lambda}{10^{44} \mathrm{erg s^{-1}}} \right)^{\beta} \left(\frac{\mathrm{FWHM_{line}}}{10^3 \mathrm{km s^{-1}}} \right)^2, \quad (2)$$

where the best-fit values for the scaling parameters α, β depend on the respective emission lines and/or monochromatic luminosity L_λ chosen. For instance, considering the Hβ line one has $\alpha = (4.4 \pm 0.2) \times 10^6$, $\beta = 0.64 \pm 0.2$ at $L_\lambda = L_{H}\beta$ or, considering the continuum luminosity at rest-frame 5100 Å, $L_{5100Å}$, it is found $\alpha = (4.7 \pm 0.3) \times 10^6$, $\beta = 0.63 \pm 0.06$ at $L_\lambda = \lambda L_{5100\,Å}$[10]. The BH masses derived from these relations can be found in Supplementary Table 3. Alternatively, we also used the relations of[138], finding a systematic rise in BH mass of about 0.15–0.2 dex. These relationships are calibrated to the most updated and robust mass determinations from reverberation mapping. The majority of reverberation mapping studies have been conducted using Hβ on low-redshift AGN[139–142]. For high-z sources, the MgII or C iv line is often utilized. However, this involves applying additional scaling from the Hβ line to formulate the virial mass based on other lines[143]. These relations have been used to measure BH masses for thousands of sources with an estimated uncertainty of about factor 2–3 (i.e. dex = 0.3–0.5[144]), when using either Hβ or MgII. Estimates based on the high ionization C iv line are even more uncertain (>0.5 dex), as this line shows large velocity offsets, implying significant non-virialized motions[145,146]. Moreover, there is mounting evidence that large C iv blueshifts (>2000 km s^{-1}) are more common at $z > 6$ than at lower redshifts[147–149]. Since the prism resolution of our data does not allow us to distinguish between the narrow and broad C iv component, either from the BLR or from outflows, we do not use the detected C iv emission line to infer the M_{BH}. We report our estimate for the BH mass of CANUCS-LRD-z8.6 from both Hβ and L_{5100} Å in Supplementary Table 3 for our fiducial fit.

From the BH mass measurements ($M_{BH,H\beta}$, $M_{BH,5100}$ Å), we calculate the Eddington luminosity:

$$L_{Edd,H}\beta/5100\,Å = 1.3 \times 10^{38} \left(\frac{M_{BH,\,H\beta/5100\,mathrmÅ}}{M_\odot} \right) \mathrm{erg\,s^{-1}} \quad (3)$$

We also compute the bolometric luminosity (L_{bol}) of the AGN using the continuum luminosity at 3000 Å and using the bolometric correction presented by ref. 150. From the L_{Edd} and L_{bol}, we derive the corresponding Eddington ratios $\lambda_{Edd} = L_{bol}/L_{Edd} = 0.1$. We report all our results in Supplementary Table 3. We find comparable quantities (within 0.2–0.5 dex) also for the Test 1 and Test 2 cases.

Spectral energy distribution fitting

We perform a spectro-photometric fit to the NIRCam photometry and NIRSpec spectroscopy using `Bagpipes`[43,44] with the primary goal of determining the stellar mass for CANUCS-LRD-z8.6. There was no need to scale the spectrum to the photometry. In the `Bagpipes` SED fitting procedure, we fix the redshift to the spectroscopic redshift of 8.63, and we assume a double power law (DPL) star formation history (SFH), Calzetti dust attenuation curve[151], and Chabrier initial mass function (IMF)[152]. The priors for the fitting parameters are reported in Supplementary Table 4. We fixed the ionization parameter to $\log(U) = -1.5$, which is derived from the 'OHNO' diagnostic (see Section "Electron temperature and metallicity"). We also set the range of metallicity considering the highest upper limit derived from observations, $Z < 0.2 Z_\odot$ (see Section "Electron temperature and metallicity"). We checked that our results do not change when increasing the upper bound of the metallicity range up to $Z = 2.5 Z_\odot$.

We adopt a Calzetti attenuation curve in the SED fitting procedure as the dust attenuation curves of high-redshift galaxies ($z > 6$) are generally found to be flat and lack a prominent UV bump feature[153,154]. In addition to using the Calzetti standard template as our fiducial dust attenuation model, we try to fit the data with an SMC template. Moreover, we adopt a flexible analytical attenuation model[153,154] to better constrain the shape of the dust attenuation curve for our object. The resulting inferred attenuation curve is Calzetti-like, though slightly shallower in the rest-frame UV. We also found that the assumed shape of the dust attenuati on curve significantly impacts the inferred V-band dust attenuation (ΔA_V ~ 0.6 dex), which in turn affects fundamental galaxy properties to a lesser extent (e.g., M_*, SFR, and stellar age by 0.2–0.4 dex) due to degeneracies. This is consistent with previous studies that conducted similar analysis[121,153,155,156].

Alongside the DPL model, which we use as our fiducial SFH model, we also perform fits with other SFHs, including the nonparametric SFHs from ref. 88 and the Leja model with a continuity prior[157], and the parametric exponentially declining SFH. We found similar results within uncertainties regardless of the SFH model choice. However, this may be an exception rather than the rule, as some studies in the literature indicate that SFH model selection can significantly impact the inferred galaxy properties[153,156–159].

Firstly, we fitted the observed SED without including an AGN contribution (no-AGN run). Therefore, to allow reliable estimates of the inferred host galaxy's properties, we subtracted from the observed spectrum the broad Hβ component, which is a clear AGN signature, using the best-fitting model shown in Figure 1. We checked that subtracting the C iv and N iv] did not change the fitting results. We did not treat the UV continuum, since the real AGN contribution in LRDs to the UV flux is still unknown, and we wanted to understand what the properties of CANUCS-LRD-z8.6 would be if all the observed UV light came from stars. Supplementary Fig. 4 shows the `Bagpipes` spectro-photometric fit in orange along with the posterior distribution of some quantities of interest and the resulting SFH. Results for the fitting parameters are reported in Supplementary Table 4. The best-fitting `Bagpipes` model is able to reproduce most of the shape of the observed spectrum of CANUCS-LRD-z8.6. However, it does not capture some features that can be ascribed to the presence of a powerful ionizing source: (i) the non-detection of [O II]3727 emission while a very bright [O III]λ5008 emission; (ii) the full Hγ-[O III]λ4364 flux; (iii) the red slope of the continuum in the optical regime; (iv) the C iv and N iv] emissions. Indeed, in this run of `Bagpipes`, the main excitement mechanism for emission lines comes from stars thus, in our case, simple stellar population (SSP) models cannot reproduce all the observed spectral features.

Consequently, we run `Bagpipes` including a model for AGN continuum, and broad Hβ[56] (AGN run). In `Bagpipes`, following ref. 160, the AGN continuum emission is modeled with a broken power law, with two spectral indices (α_λ, β_λ) and a break at $\lambda_{rest} = 5100$ Å. The broad Hβ is modeled as a Gaussian varying normalization and velocity dispersion. From this run we get $\log(M_*/M_\odot) = 9.2 \pm 0.1$, and a spectral index in the UV regime of α_λ ~ −2. The continuum slope in the UV is usually found to be within the (−2, 2) range of values[160–163] and even though α_λ ~−2 gives a good result in terms of residuals ($\chi^2_{red} = 2.2$), comparable to the no-AGN case, the posterior is hitting the edge of the prior lower limits. Therefore, we performed a run with `Bagpipes`

extending the lower range of the prior on α_λ down to −4, in order to ascertain the implications on the derived properties. In this case, we get a $\chi^2_{\rm red} = 2.0$, and the best fit α_λ is equal to -2.9 ± 0.1. The stellar mass show an increase to $\log(M_*/M_\odot) = 9.65 \pm 0.1$, while the other properties still remain consistent within errorbars with the run having $\alpha_\lambda \sim -2$. Supplementary Fig. 5 shows the `Bagpipes` spectro-photometric fit in orange along with the posterior distribution of some quantities of interest and the resulting SFH. The red continuum in the optical is captured by the best-fitting model, as well as the broad emissions. Furthermore, the [O II] emission is dimmer than in the previous run, yet it still does not align with the observed non-detection. The metallicity in both runs (w/o and with AGN) is in agreement with the observed data. The dust attenuation is about 2.2 times higher than in the previous run, causing the stellar mass to increase 0.4 dex. We did not set a tight prior on A_V since the observed value is very uncertain (see Section 22 and Supplementary Table 2); indeed it is in agreement within errors with the results of both no-AGN and AGN runs, considering that $A_V = 0.44 A_V^{\rm neb}$ assuming a Calzetti dust law[151]. However, in order to compare with the results from the no-AGN run, we run `Bagpipes` including the AGN model as before and setting a tight Gaussian prior around the value of A_V determined from the no-AGN run (AGN-tight run), and we obtained $A_V = 0.7 \pm 0.2$ and $\log(M_*/M_\odot) = 9.42 \pm 0.07$. Finally, the degeneracy between the AGN model, A_V and M_* is evident, and prevents us from obtaining a precise determination of M_*. For the aim of this work, we considered the M_* derived from the AGN-run as fiducial, and its error accounts for the uncertainties due to the variation of the SED model, i.e. $\log(M_*/M_\odot) = 9.65^{+0.1}_{-0.44}$ (corrected for magnification).

With these caveats, we propose a physical model to explain the observed properties of CANUCS-LRD-z8.6 (see also and Fig. 4 for details). Our modeling of CANUCS-LRD-z8.6 suggests an AGN-dominated UV continuum with minimal dust obscuration along our sight-line, while the red rest-optical continuum is likely due to dust-obscured stellar emission. Its compact size and high SFR (about 50–150 $M_\odot yr^{-1}$) indicate significant obscuration in stellar birth clouds. This suggests that CANUCS-LRD-z8.6 is in an evolved state that will transition toward a luminous quasar-like system at $z = 6$, rather than a lower-luminosity AGN at similar redshifts. Even though the run including the AGN component better reproduces the observed data, higher wavelength observations are needed to constrain the real AGN contribution to the observed multiwavelength light of CANUCS-LRD-z8.6. How best to incorporate AGN components in SED fitting for LRDs remains a topic of ongoing debate due to the inability of current data to meaningfully distinguish between different models[4,47,164]. In light of these uncertainties, we decided to use the stellar mass of the AGN-run and to account for the variation arising from the other models (no-AGN, AGN-tight) in the error bars.

Comparison with simulations and semi-analytical models

In this section, we investigate the possible formation channels for the massive BH powering CANUCS-LRD-z8.6 by comparing the inferred BH mass with predictions from semi-analytical models (SAM) and numerical simulations.

To get a first approximate idea about the possible growth history of the CANUCS-LRD-z8.6's BH, we first assume that this BH has been accreting for its entire history at a fixed rate, expressed as a fraction of the Eddington rate, with a constant radiative efficiency $\epsilon = 0.1$. As shown in Fig. 5, fixing the accretion rate to the observed value ($\lambda_{\rm Edd} = 0.1$) requires an extremely heavy BH mass ($M_{\rm seed} > 3 \times 10^7 M_\odot$) at redshifts higher than 25. This seed mass is higher than any value predicted by theoretical models[165]. This implies that, at earlier epochs, the BH powering CANUCS-LRD-z8.6 must have been accreted at rates higher than the one observed at $z = 8.63$.

Assuming $\lambda_{\rm Edd} = 1$ leads to a seed mass of $M_{\rm seed} \sim 10^4 M_\odot$ at $z \sim 25$ or $M_{\rm seed} \gtrsim 10^5 M_\odot$ at $z \sim 15$. This growth path is consistent both with intermediate-mass BHs formed in dense star clusters[166] and with heavy seeds predicted by the direct-collapse BH scenario[60], and/or by scenarios based on primordial black holes[167,168].

Assuming $\lambda_{\rm Edd} = 1.5$, the required seed mass would be consistent with low-mass seeds (10-100 $M_\odot$) from Pop III stellar remnants at $z \gtrsim 20$[169]. This argument suggests that the BH in CANUCS-LRD-z8.6 originates from heavy seeds, constantly growing at a pace close to Eddington, or from light seeds constantly growing at super-Eddington rates.

In the following, we discuss the formation channel of CANUCS-LRD-z8.6's BH more accurately by performing a comparison with SAM predictions. Initially, we consider the results by ref. 64, hereafter C24. This model, calibrated to match the galaxy stellar mass function in the local universe, is also able to reproduce the luminosity and stellar mass functions of galaxies up to $z \sim 9$[64], and the local $M_{\rm BH} - M_*$ relation. The C24 models are based on the GAEA SAM [e.g.,[170,171]] run on merger trees extracted by using the `PINOCCHIO` code[172], and we consider here two different seeding models: (i) Pop III.1, a scheme that allows for an early formation of massive seeds (about $10^5 M_\odot$) at $z \sim 25$ from the collapse of Pop III protostars[173]; this formation mechanism is physically motivated and does not depend on the mass resolution of the simulation; (ii) All Light Seed (ALS), a model that results into seeds of 10-100 $M_\odot$. In this model, accretion onto BHs is assumed to be Eddington-Limited. Pop III.1 stars are a subclass of Population III stars, which ref. 174 divided into two categories. Pop III.1 stars are a unique type of Population III stars that form at the centers of dark matter minihalos in the early universe ($z \gtrsim 20$), remaining isolated from any stellar or BH feedback[174]. In contrast, Pop III.2 stars also form within dark matter minihalos but are affected by feedback from external astrophysical sources. This external influence promotes gas fragmentation, leading to the formation of lower-mass stars compared to Pop III.1.

For the scope of this work, we compare CANUCS-LRD-z8.6 with the most massive BHs predicted by the C24 models at $z \sim 8$ for the two seeding prescriptions, as shown in the left panel of Supplementary Fig. 6. This comparison implies that SAMs employing Eddington-limited accretion, although successfully describing the statistical properties of galaxies and BHs from the local up to the high-z universe, fail in reproducing the most extreme BHs at high-redshift, with CANUCS-LRD-z8.6 representing one of the most extreme examples.

We further consider the results by ref. 69, which investigates the formation of massive BHs at $z > 7$ by means of the SAM Cosmic Archaeology Tool (CAT)[68]. In this work, the seeding prescription accounts for both light and heavy seeds, and the BH growth can occur in the Eddington-limited (EL) and super-Eddington (SE) regimes. As can be seen from the left panel of Supplementary Fig. 6, in the CAT framework, the EL model predicts BH masses that are consistent with GNz-11 at $z \sim 10$ and CEERS-1019 at $z \sim 8.7$[41], but do not exceed about $10^7 M_\odot$, therefore being inconsistent with our new data. The model including SE accretion predicts several tracks that successfully assemble $10^8 M_\odot$ at $z = 8.6$[69], the most massive one shown in blue in the left panel of Fig. 5. Thus, super-Eddington accretion is essential to assemble a large amount of mass within 500 Myr (see also refs. 175,176) and therefore to reproduce the CANUCS-LRD-z8.6 inferred mass.

The main caveat of SAMs is that they cannot fully capture the complex and non-linear interplay between BH accretion and feedback processes. Therefore, the growth predicted in SAMs during the SE phase might be too efficient, if compared to more sophisticated models, e.g. hydrodynamical numerical simulations. This is clearly shown by the results of refs. 177,178 that are based on numerical simulations with light seeds growing at super-Eddington pace. From refs. 177,178 results, it can be seen that early light seeds, even if accreting at super-Eddington rate, can reach a maximum mass of $10^5 M_\odot$ ($10^7 M_\odot$) at $z \sim 6$, thus being unable to reproduce the BH masses estimated so far at $z > 6$. For this reason, most of the numerical hydrodynamical simulations of BH formation and growth assume a heavy

seed prescription ($M_{seed} > 10^5 M_\odot$) to reproduce the large masses of BHs powering $z \sim 6$ quasars. The accretion rate onto the BHs is modeled according to the Bondi–Hoyle–Lyttleton prescription[179–181], with a boost factor α used as a correction factor for the spatial resolution of the gas distribution surrounding the BH.

In what follows, we separately discuss predictions from simulations that cap the BH accretion to the Eddington limit and those that allow for super-Eddington growth. In the middle panel of Supplementary Fig. 6, we report the results of EL simulations. We find that the only simulation that can reproduce the CANUCS-LRD-z8.6 BH mass is the reference run by ref. 177. Vice-versa, both ref. 72, when using the numerical recipe of the FABLE suite[71], and ref. 182 predict a BH mass that is about 1 order of magnitude smaller. Interestingly, all the simulations reported in this panel, though being inconsistent with CANUCS-LRD-z8.6, are capable of reproducing AGN candidates such as GNz-11 at z-10 and CEERS-1019 at $z \sim 8.7$[41], and the estimated masses of BHs powering z-6 quasars, apart from the most extreme case of J0100+2802 ($M_{BH} \sim 10^{10} M_\odot$,[15]). We further notice that the simulations by[177] predict a BH mass at z-8 that is about 2 orders of magnitude smaller with respect to the reference run, if a radiative efficiency larger than only a factor of two is considered. This clearly shows how sensitive predictions from numerical simulations are to the feedback prescriptions implemented.

We now move to numerical simulations of heavy BH seeds' growth, including super-Eddington accretion, shown in the right panel of Supplementary Fig. 6. First of all, we note that the reference run by ref. 72 is able to reproduce not only CANUCS-LRD-z8.6 but also $z \sim 6$ quasars, including the extreme case of J0100+2802. With respect to the original recipe employed in the FABLE suite (shown in the middle panel), in the reference run the authors apply the following variations: (i) reduce the halo mass where BH seeds are placed (from $M_h = 5 \times 10^{10} h^{-1}\,M_\odot$ to $M_h = \times 10^9 h^{-1}\,M_\odot$), effectively resulting in earlier BH seeding (from $z \sim 13$ to $z \sim 18$); (ii) reduce the overall AGN feedback; (iii) allow for mild super-Eddington accretion ($\lambda_{Edd} = 2$). All these changes promote early BH growth, which emerges as a necessary condition to explain the BH mass of early AGN and quasars. Interestingly, this simulation supports a scenario in which CANUCS-LRD-z8.6 represents a progenitor of the most massive QSOs at $z > 6$, such as J0100+2802.

We further notice that the run *Bh22d* of ref. 182 (see also the similar setup used in ref. 183) predicts a rapid mass assembly consistent with CANUCS-LRD-z8.6, if the accretion rate is boosted ($\lambda_{Edd} = 2$, $\alpha = 100$) and the radiative efficiency is low ($\epsilon = 0.1$), which in turn lowers the AGN feedback effect on the BH growth. Similarly, refs. 177,184 find the AGN feedback to be the most limiting factor in BH growth.

Notably, in ref. 177, the BH grows less in the super-Eddington regime due to the excessive feedback. However, this conclusion is sensitive to the detailed numerical implementation. Reference 185 explored the BH growth with high-resolution numerical simulations with a comprehensive model of AGN feedback in the super-Eddington regime. They find that the jet power in the super-Eddington regime is a critical factor in regulating the accretion rate onto the BH, because of its ability to remove the fueling gas, as also found in other works[186]. Their run with low feedback predicts a BH mass at $z \sim 8.5$, only a factor of about 2 smaller than CANUCS-LRD-z8.6.

We further compare model predictions with the stellar mass inferred for CANUCS. The CAT model, including SE accretion, predicts systems with black holes over-massive with respect to their host galaxy when compared to the local MBH–M^* relation70. This is a consequence of a de-coupled evolution between the BH and the galaxy, triggered after short (0.5–3 Myr), (1–4%) phases of SE accretion during which the BH experiences fast growth and suppresses star formation via efficient feedback, a scenario that is also supported by recent simulations[52] and observations of quiescent over-massive black holes[53]. Interestingly, the stellar masses predicted by CAT at $z \sim 9$ are consistent with the low-mass end of the estimated stellar mass for CANUCS-LRD-z8.6. Regarding numerical simulations, the reference model in ref. 177 also successfully assembles $>10^{10} M_\odot$ by $z \sim 9$, satisfying the constraints posed by CANUCS-LRD-z8.6 both in terms of black hole mass and stellar mass assembly at $z = 8.6$. To our knowledge, none of the other models explored in this overview are able to satisfy both constraints, although for many of them we were not able to recover the information on the stellar mass from their published works.

The comparison among results from different numerical simulations emphasizes how complex is the modeling of BH seeding, accretion rate, and AGN feedback, and how important it is to collect observational data as the one provided in this work. CANUCS-LRD-z8.6 poses significant challenges to both hydrodynamical simulations and semi-analytical models. Its existence requires rapid and efficient assembling of $10^8 M_\odot$ in only 500 Myr, thus providing stringent constraints to seeding prescriptions, feedback recipes, and accretion physics modeling in theoretical models and simulations.

Data availability

The raw data for CANUCS-LRD-z8.6 used in this work are publicly available and accessible in the Mikulski Archive for Space Telescopes (MAST) archive (https://doi.org/10.17909/rfcj-5910), selecting the Project ID 1208, NIRSpec MSA and the cluster MACS1149. Catalogs and data are also available in the first public CANUCS data release (https://niriss.github.io/data_release1.html). Source data to reproduce all data and models in the figures and tables are publicly available on Zenodo at the following (https://zenodo.org/records/15837927). The datasets generated during and/or analysed during the current study are also available from the corresponding author upon request. Data has been reduced and analyzed using the software/tools listed in the 'Code Availability' section.

Code availability

Data have been reduced using the JWST Science Calibration pipeline available at https://github.com/spacetelescope/jwstand described at https://jwst-docs.stsci.edu/jwst-science-calibration-pipeline#gsc.tab=0. The modified version of Detector1Pipeline is available on request by contacting Dr. Sarrouh at gsarrouh@yorku.ca. The authors made extensive use of the following publicly available tools/software to carry out the analysis presented in this work: Jupyter Notebook (https://jupyter.org), Grizli (https://github.com/gbrammer/grizli), Pyneb (https://pypi.org/project/pyneb/), Bagpipes (https://bagpipes.readthedocs.io/en/latest/), GalFit (https://users.obs.carnegiescience.edu/peng/work/galfit/galfit.html), DenseBasis (https://dense-basis.readthedocs.io/en/latest/), Lenstool (https://projets.lam.fr/projects/lenstool/wiki). A specific Jupyter notebook is not needed for the analysis. Custom notebooks can be created in order to use the other tools enlisted above.

References

1. Kokorev, V. et al. UNCOVER: a NIRSpec identification of a broad-line AGN at z = 8.50. *ApJ* **957**, L7 (2023).
2. Matthee, J. et al. Little Red dots: an abundant population of faint active galactic nuclei at z ~ 5 revealed by the EIGER and FRESCO JWST surveys. *ApJ* **963**, 129 (2024).
3. Taylor, A. J. et al. Broad-Line AGN at 3.5 < z < 6: The black hole mass function and a connection with little red dots. *ApJ*, **986**, 165 (2025).
4. Wang, B. et al. RUBIES: evolved stellar populations with extended formation histories at z ~ 7-8 in candidate massive galaxies identified with JWST/NIRSpec. *ApJ* **969**, L13 (2024).
5. Durodola, E., Pacucci, F. & Hickox, R. C. Exploring the AGN fraction of a sample of JWST's little red dots at 5 < z < 8: overmassive black holes are strongly favored. *ApJ*, **985**, 169 (2025).

6. Silk, J., Begelman, M. C., Norman, C., Nusser, A. & Wyse, R. F. G. Which came first: supermassive black holes or galaxies? Insights from JWST. *ApJ* **961**, L39 (2024).
7. Planck Collaboration. et al. Planck 2018 results. VI. Cosmological parameters. *Astron. Astrophys.* **641**, A6 (2020).
8. Desprez, G. et al. ΛCDM not dead yet: massive high-z Balmer break galaxies are less common than previously reported. *MNRAS* **530**, 2935–2952 (2024).
9. Kocevski, D. D. et al. The rise of faint, Red Active Galactic Nuclei at $z > 4$: a sample of Little Red Dots in the JWST extragalactic legacy fields. *ApJ*, **986**, 126 (2025).
10. Greene, J. E. & Ho, L. C. Estimating black hole masses in active galaxies using the Hα emission line. *ApJ* **630**, 122–129 (2005).
11. Feltre, A., Charlot, S. & Gutkin, J. Nuclear activity versus star formation: emission-line diagnostics at ultraviolet and optical wavelengths. *MNRAS* **456**, 3354–3374 (2016).
12. Scholtz, J. et al. JADES: a large population of obscured, narrow line AGN at high redshift. *A&A*, **697**, A175 (2025).
13. Treiber, H. et al. UNCOVERing the high-redshift AGN population among extreme UV line emitters. *ApJ*, **984**, 93 (2025).
14. Topping, M. W. et al. Metal-poor star formation at z > 6 with JWST: new insight into hard radiation fields and nitrogen enrichment on 20 pc scales. *MNRAS* **529**, 3301–3322 (2024).
15. Mazzucchelli, C. et al. XQR-30: black hole masses and accretion rates of 42 $z \gtrsim 6$ quasars. *Astron. Astrophys.* **676**, A71 (2023).
16. D'Odorico, V. et al. XQR-30: the ultimate XSHOOTER quasar sample at the reionization epoch. *MNRAS* **523**, 1399–1420 (2023).
17. Bunker, A. J. et al. JADES NIRSpec spectroscopy of GN-z11: Lyman-α emission and possible enhanced nitrogen abundance in a z = 10.60 luminous galaxy. *Astron. Astrophys.* **677**, A88 (2023).
18. Maiolino, R. et al. A small and vigorous black hole in the early Universe. *Nature* **627**, 59–63 (2024).
19. D'Eugenio, F. et al. JADES: carbon enrichment 350 Myr after the Big Bang. *Astron. Astrophys.* **689**, A152 (2024).
20. Castellano, M. et al. JWST NIRSpec spectroscopy of the remarkable bright galaxy GHZ2/GLASS-z12 at redshift 12.34. *ApJ* **972**, 143 (2024).
21. Übler, H. et al. GA-NIFS: JWST discovers an offset AGN 740 million years after the Big Bang. *MNRAS* **531**, 355–365 (2024).
22. Stark, D. P. et al. Spectroscopic detection of C IV λ1548 in a galaxy at z = 7.045: implications for the ionizing spectra of reionization-era galaxies. *MNRAS* **454**, 1393–1403 (2015).
23. Schindler, J.-T. et al. A broad-line, low-luminosity active galactic nucleus at $z = 7.3$ anchoring a large galaxy overdensity. *Nat. Astronom.* (2025).
24. Akins, H. B. et al. Strong rest-UV emission lines in a "little red dot" AGN at $z = 7$: early SMBH growth alongside compact massive star formation? *ApJL* **980**, L29 (2025).
25. Bañados, E. et al. An 800-million-solar-mass black hole in a significantly neutral Universe at a redshift of 7.5. *Nature* **553**, 473–476 (2018).
26. Greig, B., Mesinger, A. & Bañados, E. Constraints on reionization from the z = 7.5 QSO ULASJ1342+0928. *MNRAS* **484**, 5094–5101 (2019).
27. Totani, T. et al. Implications for cosmic reionization from the optical afterglow spectrum of the gamma-ray burst 050904 at z = 6.3*. *PASJ* **58**, 485–498 (2006).
28. Binette, L. et al. Constraints on the densities and temperature of the Seyfert 2 narrow line region. *AA* **684**, A53 (2024).
29. Curti, M. et al. The chemical enrichment in the early Universe as probed by JWST via direct metallicity measurements at z ~ 8. *MNRAS* **518**, 425–438 (2023).
30. Curti, M. et al. JADES: the star-formation and chemical enrichment history of a luminous galaxy at z 9.43 probed by ultra-deep JWST/NIRSpec spectroscopy. *A&A* **697**, A89 (2025).
31. Baskin, A. & Laor, A. What controls the [OIII]λ5007 line strength in active galactic nuclei? *MNRAS* **358**, 1043–1054 (2005).
32. Mazzolari, G. et al. New AGN diagnostic diagrams based on the [OIII]λ4363 auroral line. *A&A* **691**, A345 (2024).
33. Cameron, A. J. et al. JADES: probing interstellar medium conditions at $z \sim 5.5 - 9.5$ with ultra-deep JWST/NIRSpec spectroscopy. *Astron. Astrophys.* **677**, A115 (2023).
34. Balmaverde, B. & Capetti, A. The naked nuclei of low ionization nuclear emission line regions. *Astron. Astrophys.* **581**, A76 (2015).
35. Maiolino, R. et al. JWST meets Chandra: a large population of Compton-thick, feedback-free, and intrinsically X-ray weak AGN, with a sprinkle of SNe. *MNRAS* (2025).
36. Juodžbalis, I. et al. JADES—The Rosetta Stone of JWST-discovered AGN: deciphering the intriguing nature of early AGN. *MNRAS* (2024).
37. Yue, M. et al. Stacking X-ray observations of "Little Red Dots": Implications for their active galactic nucleus properties. *ApJ* **974**, L26 (2024).
38. Marconi, A. et al. HOMERUN: a new approach to photoionization modeling: I. Reproducing observed emission lines with percent accuracy and obtaining accurate physical properties of the ionized gas. *Astron. Astrophys.* **689**, A78 (2024).
39. Backhaus, B. E. et al. CLEAR: emission-line ratios at cosmic high noon. *ApJ* **926**, 161 (2022).
40. Cleri, N. J. et al. CLEAR: paschen-β star formation rates and dust attenuation of low-redshift galaxies. *ApJ* **929**, 3 (2022).
41. Larson, R. L. et al. A CEERS discovery of an accreting supermassive black hole 570 Myr after the Big Bang: identifying a progenitor of massive z > 6 quasars. *ApJ* **953**, L29 (2023).
42. Trussler, J. A. A. et al. Seeing sharper and deeper: JWST's first glimpse of the photometric and spectroscopic properties of galaxies in the epoch of reionization. *MNRAS* **523**, 3423–3440 (2023).
43. Carnall, A. C., McLure, R. J., Dunlop, J. S. & Davé, R. Inferring the star formation histories of massive quiescent galaxies with BAGPIPES: evidence for multiple quenching mechanisms. *MNRAS* **480**, 4379–4401 (2018).
44. Carnall, A. C. et al. How to measure galaxy star formation histories. I. Parametric models. *ApJ* **873**, 44 (2019).
45. Ji, X. et al. GA-NIFS: an extremely nitrogen-loud and chemically stratified galaxy at $z \sim 5.55$. *MNRAS* **535**, 881 (2024).
46. Isobe, Y. et al. JADES: average nitrogen enhancement in high-redshift broad-line active galactic nuclei. *MNRAS* **541**, L71–L79 (2025).
47. Casey, C. M. et al. Dust in little red dots. *ApJ* **975**, L4 (2024).
48. Nenkova, M., Sirocky, M. M., Nikutta, R., Ivezić, Ž. & Elitzur, M. AGN Dusty Tori. II. Observational implications of clumpiness. *ApJ* **685**, 160–180 (2008).
49. Hönig, S. F. Tori, discs, and winds: the first ten years of AGN interferometry. In Boffin, H. M. J., Hussain, G., Berger, J.-P. & Schmidtobreick, L. (eds.) *Astronomy at High Angular Resolution*, vol. 439 of *Astrophysics and Space Science Library*, **95** (2016).
50. García-Burillo, S. et al. The Galaxy Activity, Torus, and Outflow Survey (GATOS). I. ALMA images of dusty molecular tori in Seyfert galaxies. *Astron. Astrophys.* **652**, A98 (2021).
51. Reines, A. E. & Volonteri, M. Relations between central black hole mass and total galaxy stellar mass in the local universe. *ApJ* **813**, 82 (2015).
52. Huško, F. et al. The effects of super-Eddington accretion and feedback on the growth of early supermassive black holes and galaxies. *MNRAS* **537**, 2559–2578 (2025).
53. Juodžbalis, I. et al. A dormant overmassive black hole in the early Universe. *Nature* **636**, 594–597 (2024).

54. Li, J. et al. Tip of the iceberg: overmassive black holes at 4 < z < 7 found by JWST are not inconsistent with the local <inline-formula></inline-formula> relation. *ApJ* **981**, 19 (2025).
55. Maiolino, R. et al. JADES. The diverse population of infant Black Holes at 4<z<11: merging, tiny, poor, but mighty. *A&A* **691**, A145 (2024).
56. Carnall, A. C. et al. A massive quiescent galaxy at redshift 4.658. *Nature* **619**, 716–719 (2023).
57. Weibel, A. et al. RUBIES reveals a massive quiescent galaxy at z=7.3. *ApJ* **983**, 11 (2025).
58. Bogdán, Á. et al. Evidence for heavy-seed origin of early supermassive black holes from a z ≈ 10 X-ray quasar. *Nat. Astron.* **8**, 126–133 (2024).
59. Huang, H.-L., Jiang, J.-Q., He, J., Wang, Y.-T. & Piao, Y.-S. Sub-Eddington accreting supermassive primordial black holes explain Little Red Dots. Preprint at https://doi.org/10.48550/arXiv.2410.20663 (2024).
60. Bromm, V. & Loeb, A. Formation of the first supermassive black holes. *Astrophys. J.* **596**, 34–46 (2003).
61. Maio, U., Borgani, S., Ciardi, B. & Petkova, M. The seeds of supermassive black holes and the role of local radiation and metal spreading. *Publ. Astron. Soc. Aust.* **36**, e020 (2019).
62. Bhowmick, A. K. et al. Impact of gas spin and Lyman-Werner flux on black hole seed formation in cosmological simulations: implications for direct collapse. *Mon. Not. R. Astron. Soc.* **510**, 177–196 (2022).
63. Singh, J., Monaco, P. & Tan, J. C. The formation of supermassive black holes from Population III.1 seeds. II. Evolution to the local universe. *MNRAS* **525**, 969–982 (2023).
64. Cammelli, V. et al. The formation of supermassive black holes from Population III.1 seeds. III. Galaxy evolution and black hole growth from semi-analytic modelling. *MNRAS* **536**, 851–870 (2025).
65. Heger, A. & Woosley, S. E. The nucleosynthetic signature of population III. *ApJ* **567**, 532–543 (2002).
66. O'Shea, B. W., Abel, T., Whalen, D. & Norman, M. L. Forming a primordial star in a relic H II region. *Astrophys. J. Lett.* **628**, L5–L8 (2005).
67. Jeon, J., Liu, B., Bromm, V. & Finkelstein, S. L. Observability of low-luminosity AGN in the early universe with JWST. *MNRAS* **524**, 176 (2023).
68. Trinca, A. et al. The low-end of the black hole mass function at cosmic dawn. *MNRAS* **511**, 616–640 (2022).
69. Schneider, R. et al. Are we surprised to find SMBHs with JWST at z ≥ 9? *MNRAS* **526**, 3250–3261 (2023).
70. Trinca, A. et al. Episodic super-Eddington accretion as a clue to overmassive black holes in the early universe. Preprint at https://doi.org/10.48550/arXiv.2412.14248 (2024).
71. Henden, N. A., Puchwein, E., Shen, S. & Sijacki, D. The FABLE simulations: a feedback model for galaxies, groups, and clusters. *MNRAS* **479**, 5385–5412 (2018).
72. Bennett, J. S., Sijacki, D., Costa, T., Laporte, N. & Witten, C. The growth of the gargantuan black holes powering high-redshift quasars and their impact on the formation of early galaxies and protoclusters. *MNRAS* **527**, 1033–1054 (2024).
73. Willott, C. J. et al. The near-infrared imager and slitless spectrograph for the James Webb Space Telescope. II. Wide field slitless spectroscopy. *PASP* **134**, 025002 (2022).
74. Soucail, G., Fort, B., Mellier, Y. & Picat, J. P. A blue ring-like structure in the center of the A 370 cluster of galaxies. *Astron. Astrophys.* **172**, L14–L16 (1987).
75. Ebeling, H., Edge, A. C. & Henry, J. P. MACS: a quest for the most massive galaxy clusters in the universe. *ApJ* **553**, 668–676 (2001).
76. Lotz, J. M. et al. The frontier fields: survey design and initial results. *ApJ* **837**, 97 (2017).
77. Sarrouh, G. T. E. et al. CANUCS/technicolor data release 1: imaging, photometry, slit spectroscopy, and stellar population parameters. Preprint at https://doi.org/10.48550/arXiv.2506.21685 (2025).
78. Noirot, G. et al. The first large catalogue of spectroscopic redshifts in Webb's first deep field, SMACS J0723.3-7327. *MNRAS* **525**, 1867–1884 (2023).
79. Willott, C. J. et al. A steep decline in the galaxy space density beyond Redshift 9 in the CANUCS UV luminosity function. *ApJ* **966**, 74 (2024).
80. Asada, Y. et al. Improving photometric redshifts of Epoch of Reionization galaxies: a new transmission curve with the neutral hydrogen damped Lyα absorption. *Astrophys. J. Lett.* **983**, L2 (2024).
81. Sarrouh, G. T. E. et al. Exposing line emission: the systematic differences of measuring galaxy stellar masses with JWST NIRCam medium versus wide band photometry. *ApJ* **967**, L17 (2024).
82. Martis, N. S. et al. Modeling and subtracting diffuse cluster light in JWST images: a relation between the spatial distribution of globular clusters, dwarf galaxies, and intracluster light in the lensing cluster SMACS 0723. *ApJ* **975**, 76 (2024).
83. Brammer, G. & Matharu, J. gbrammer/grizli: Release 2021 (2021).
84. Bradley, L. et al. astropy/photutils: 1.6.0 (2022).
85. Ferruit, P. et al. The Near-Infrared Spectrograph (NIRSpec) on the James Webb Space Telescope. II. Multi-object spectroscopy (MOS). *Astron. Astrophys.* **661**, A81 (2022).
86. Brammer, G. msaexp: NIRSpec analysis tools (2022).
87. Jullo, E. et al. A Bayesian approach to strong lensing modelling of galaxy clusters. *N. J. Phys.* **9**, 447 (2007).
88. Iyer, K. G. et al. Nonparametric star formation history reconstruction with Gaussian processes. I. Counting major episodes of star formation. *ApJ* **879**, 116 (2019).
89. McGaugh, S. S. & Schombert, J. M. Weighing galaxy disks with the Baryonic Tully-Fisher relation. *ApJ* **802**, 18 (2015).
90. Elíasdóttir, Á. et al. Where is the matter in the Merging Cluster Abell 2218? Preprint at https://doi.org/10.48550/arXiv.0710.5636 (2007).
91. Peng, C. Y., Ho, L. C., Impey, C. D. & Rix, H.-W. Detailed decomposition of galaxy images. II. Beyond axisymmetric models. *AJ* **139**, 2097–2129 (2010).
92. Birrer, S., Amara, A. & Refregier, A. Gravitational lens modeling with basis sets. *ApJ* **813**, 102 (2015).
93. Birrer, S. & Amara, A. Lenstronomy: multi-purpose gravitational lens modelling software package. *Phys. Dark Universe* **22**, 189–201 (2018).
94. Yang, L., Birrer, S. & Treu, T. A versatile tool for cluster lensing source reconstruction—I. Methodology and illustration on sources in the Hubble Frontier Field Cluster MACS J0717.5+3745. *MNRAS* **496**, 2648–2662 (2020).
95. Greig, B. et al. Blind QSO reconstruction challenge: exploring methods to reconstruct the Ly α emission line of QSOs. *MNRAS* **533**, 3312–3343 (2024).
96. Umeda, H. et al. JWST measurements of neutral hydrogen fractions and ionized bubble sizes at z = 7–12 obtained with Lyα damping wing absorptions in 27 bright continuum galaxies. *ApJ* **971**, 124 (2024).
97. Trefoloni, B. et al. The missing FeII bump in faint JWST AGN: possible evidence for metal-poor broad-line regions at early cosmic times. *A&A* **700**, A203 (2025).
98. Foreman-Mackey, D., Hogg, D. W., Lang, D. & Goodman, J. emcee: The MCMC Hammer. *PASP* **125**, 306 (2013).
99. Jakobsen, P. et al. The Near-Infrared Spectrograph (NIRSpec) on the James Webb Space Telescope. I. Overview of the instrument and its capabilities. *Astron. Astrophys.* **661**, A80 (2022).

100. Calzetti, D., Kinney, A. L. & Storchi-Bergmann, T. Dust obscuration in starburst galaxies from near-infrared spectroscopy. *ApJ* **458**, 132 (1996).
101. Luridiana, V., Morisset, C. & Shaw, R. A. PyNeb: a new tool for analyzing emission lines. I. Code description and validation of results. *Astron. Astrophys.* **573**, A42 (2015).
102. Storey, P. J. & Hummer, D. G. Recombination line intensities for hydrogenic ions-IV. Total recombination coefficients and machine-readable tables for Z=1 to 8. *MNRAS* **272**, 41–48 (1995).
103. Izotov, Y. I., Stasińska, G., Meynet, G., Guseva, N. G. & Thuan, T. X. The chemical composition of metal-poor emission-line galaxies in the Data Release 3 of the Sloan Digital Sky Survey. *AA* **448**, 955–970 (2006).
104. Curti, M. et al. New fully empirical calibrations of strong-line metallicity indicators in star-forming galaxies. *MNRAS* **465**, 1384–1400 (2017).
105. Maiolino, R. & Mannucci, F. De re metallica: the cosmic chemical evolution of galaxies. *Astron. Astrophys. Rev.* **27**, 3 (2019).
106. Sanders, R. L., Shapley, A. E., Topping, M. W., Reddy, N. A. & Brammer, G. B. Direct T_e-based metallicities of z=2-9 galaxies with JWST/NIRSpec: empirical metallicity calibrations applicable from reionization to cosmic noon. *ApJ* **962**, 24 (2024).
107. Nicholls, D. C., Kewley, L. J. & Sutherland, R. S. Estimating electron temperatures in ionized nebulae: the direct method and its limitations. *PASP* **132**, 033001 (2020).
108. Katz, H. et al. First insights into the ISM at z > 8 with JWST: possible physical implications of a high [O III] λ4363/[O III] λ5007. *MNRAS* **518**, 592–603 (2023).
109. Mowla, L. et al. Formation of a low-mass galaxy from star clusters in a 600-million-year-old Universe. *Natur* **636**, 332 (2024).
110. Kokorev, V. et al. Silencing the giant: evidence of active galactic nucleus feedback and quenching in a Little Red Dot at z = 4.13. *ApJ* **975**, 178 (2024).
111. Nagao, T., Murayama, T. & Taniguchi, Y. The narrow-line region of Seyfert galaxies: narrow-line Seyfert 1 galaxies versus broad-line Seyfert 1 galaxies. *ApJ* **546**, 744–758 (2001).
112. Binette, L. et al. Temperature discrepancy with photoionization models of the narrow-line region. *Rev. Mexicana Astron. Astrofis.* **58**, 133–153 (2022).
113. Perna, M., Lanzuisi, G., Brusa, M., Mignoli, M. & Cresci, G. An X-ray/SDSS sample. I. Multi-phase outflow incidence and dependence on AGN luminosity. *Astron. Astrophys.* **603**, A99 (2017).
114. Brinchmann, J. High-z galaxies with JWST and local analogues—it is not only star formation. *MNRAS* **525**, 2087–2106 (2023).
115. Abazajian, K. N. et al. The Seventh Data Release of the Sloan Digital Sky Survey. *ApJs* **182**, 543–558 (2009).
116. Brinchmann, J. et al. The physical properties of star-forming galaxies in the low-redshift Universe. *MNRAS* **351**, 1151–1179 (2004).
117. Campbell, A., Terlevich, R. & Melnick, J. The stellar populations and evolution of H II galaxies—I. High signal-to-noise optical spectroscopy. *MNRAS* **223**, 811–825 (1986).
118. Berg, D. A., Erb, D. K., Auger, M. W., Pettini, M. & Brammer, G. B. A window on the earliest star formation: extreme photoionization conditions of a high-ionization, low-metallicity lensed galaxy at z ~ 2*. *ApJ* **859**, 164 (2018).
119. Berg, D. A. et al. Characterizing extreme emission-line galaxies. I. A four-zone ionization model for very high-ionization emission. *ApJ* **922**, 170 (2021).
120. Abazajian, K. et al. The second data release of the Sloan Digital Sky Survey. *AJ* **128**, 502–512 (2004).
121. Reddy, N. A. et al. The MOSDEF Survey: measurements of Balmer decrements and the dust attenuation curve at redshifts z ~1.4-2.6. *ApJ* **806**, 259 (2015).
122. Kriek, M. et al. The MOSFIRE Deep Evolution Field (MOSDEF) Survey: rest-frame optical spectroscopy for ~1500 H-selected galaxies at 1.37 < z < 3.8. *ApJs* **218**, 15 (2015).
123. Tripodi, R. et al. Spatially resolved emission lines in galaxies at 4≤z<10 from the JADES survey: evidence for enhanced central star formation. *Astron. Astrophys.* **692**, A184 (2024).
124. Curti, M. et al. The KLEVER Survey: spatially resolved metallicity maps and gradients in a sample of 1.2 < z < 2.5 lensed galaxies. *MNRAS* **492**, 821–842 (2020).
125. Nakajima, K. et al. JWST census for the mass-metallicity star formation relations at z = 4-10 with self-consistent flux calibration and proper metallicity calibrators. *ApJs* **269**, 33 (2023).
126. Kuraszkiewicz, J. K. et al. Emission line properties of active galactic nuclei from a post-COSTAR Hubble Space Telescope Faint Object Spectrograph Spectral Atlas. *ApJs* **150**, 165–180 (2004).
127. Nagao, T., Maiolino, R. & Marconi, A. Gas metallicity diagnostics in star-forming galaxies. *Astron. Astrophys.* **459**, 85–101 (2006).
128. Cleri, N. J. et al. Using [Ne V]/[Ne III] to understand the nature of extreme-ionization galaxies. *ApJ* **953**, 10 (2023).
129. Grazian, A. et al. On the AGN nature of two UV-bright sources at z_{spec} ~ 5.5 in the CANDELS fields: an update on the AGN space density at M_{1450}~– 22.5. *ApJ* **897**, 94 (2020).
130. Übler, H. et al. GA-NIFS: a massive black hole in a low-metallicity AGN at z ~ 5.55 revealed by JWST/NIRSpec IFS. *AA* **677**, A145 (2023).
131. Vanzella, E. et al. The unusual N IV] -emitter galaxy GDS J033218.92-275302.7: star formation or AGN-driven winds from a massive galaxy at z = 5.56. *Astron. Astrophys.* **513**, A20 (2010).
132. Glikman, E., Djorgovski, S. G., Stern, D., Bogosavljević, M. & Mahabal, A. Discovery of two spectroscopically peculiar, low-luminosity quasars at z~4. *ApJ* **663**, L73–L76 (2007).
133. Isobe, Y. et al. JWST identification of extremely low C/N Galaxies with [N/O] $\gtrsim$ 0.5 at z 6-10 evidencing the early CNO-cycle enrichment and a connection with globular cluster formation. *ApJ* **959**, 100 (2023).
134. D'Orazi, V. et al. Lithium and proton-capture elements in globular cluster dwarfs: the case of 47 TUC. *ApJ* **713**, L1–L5 (2010).
135. Maeder, A., Meynet, G. & Chiappini, C. The first stars: CEMP-no stars and signatures of spinstars. *AA* **576**, A56 (2015).
136. Charbonnel, C. et al. N-enhancement in GN-z11: first evidence for supermassive stars nucleosynthesis in proto-globular clusters-like conditions at high redshift? *Astron. Astrophys.* **673**, L7 (2023).
137. Watanabe, K. et al. EMPRESS. XIII. Chemical enrichment of young galaxies near and far at z ~ 0 and 4–10: Fe/O, Ar/O, S/O, and N/O measurements with a comparison of chemical evolution models. *ApJ* **962**, 50 (2024).
138. Vestergaard, M. & Osmer, P. S. Mass functions of the active black holes in Distant Quasars from the Large Bright Quasar Survey, the Bright Quasar Survey, and the color-selected sample of the SDSS fall equatorial stripe. *ApJ* **699**, 800–816 (2009).
139. Bentz, M. C. et al. The low-luminosity end of the radius-luminosity relationship for active galactic nuclei. *ApJ* **767**, 149 (2013).
140. Barth, A. J. et al. The Lick AGN Monitoring Project 2011: spectroscopic campaign and emission-line light curves. *ApJs* **217**, 26 (2015).
141. Grier, C. J. et al. The Sloan Digital Sky Survey Reverberation Mapping Project: Hα and Hβ reverberation measurements from first-year spectroscopy and photometry. *ApJ* **851**, 21 (2017).
142. Malik, U. et al. OzDES Reverberation Mapping Program: Hβ lags from the 6-yr survey. *MNRAS* **520**, 2009–2023 (2023).
143. Shen, Y. et al. A catalog of Quasar properties from Sloan Digital Sky Survey data release 7. *ApJs* **194**, 45 (2011).
144. Shen, Y., Liu, X., Loeb, A. & Tremaine, S. Constraining Sub-parsec binary supermassive black holes in Quasars with multi-epoch

spectroscopy. I. The General Quasar Population. *ApJ* **775**, 49 (2013).
145. Mejía-Restrepo, J. E., Trakhtenbrot, B., Lira, P. & Netzer, H. Can we improve C IV-based single-epoch black hole mass estimations? *MNRAS* **478**, 1929–1941 (2018).
146. Park, D. et al. Extending the calibration of C IV-based single-epoch black hole mass estimators for active galactic nuclei. *ApJ* **839**, 93 (2017).
147. Meyer, R. A., Bosman, S. E. I. & Ellis, R. S. New constraints on quasar evolution: broad-line velocity shifts over $1.5 \lesssim z \lesssim 7.5$. *MNRAS* **487**, 3305–3323 (2019).
148. Schindler, J.-T. et al. The X-SHOOTER/ALMA sample of quasars in the epoch of reionization. I. NIR spectral modeling, iron enrichment, and broad emission line properties. *ApJ* **905**, 51 (2020).
149. Matthews, J. H. et al. A disc wind model for blueshifts in quasar broad emission lines. *MNRAS* **526**, 3967–3986 (2023).
150. Richards, G. T. et al. Eight-dimensional mid-infrared/optical Bayesian Quasar selection. *AJ* **137**, 3884–3899 (2009).
151. Calzetti, D. et al. The dust content and opacity of actively star-forming galaxies. *ApJ* **533**, 682–695 (2000).
152. Chabrier, G. Galactic stellar and substellar initial mass function. *PASP* **115**, 763–795 (2003).
153. Markov, V. et al. Dust attenuation law in JWST galaxies at z ~ 7-8. *Astron. Astrophys.* **679**, A12 (2023).
154. Markov, V. et al. The evolution of dust attenuation in z ~ 2-12 galaxies observed by JWST. *NatAs* **9**, 458 (2025).
155. Salim, S. et al. GALEX-SDSS-WISE Legacy Catalog (GSWLC): star formation rates, stellar masses, and dust attenuations of 700,000 low-redshift galaxies. *ApJs* **227**, 2 (2016).
156. Topping, M. W. et al. Searching for extremely blue UV continuum slopes at z = 7-11 in JWST/NIRCam imaging: implications for stellar metallicity and ionizing photon escape in early galaxies. *ApJ* **941**, 153 (2022).
157. Leja, J., Carnall, A. C., Johnson, B. D., Conroy, C. & Speagle, J. S. How to measure galaxy star formation histories. II. Nonparametric models. *ApJ* **876**, 3 (2019).
158. Topping, M. W. et al. The MOSDEF-LRIS Survey: The connection between massive stars and ionized gas in individual galaxies at z ~ 2. *MNRAS* **499**, 1652–1665 (2020).
159. Whitler, L. et al. Star formation histories of UV-luminous galaxies at *z*~6.8: implications for stellar mass assembly at early cosmic times. *MNRAS* **519**, 5859–5881 (2023).
160. Vanden Berk, D. E. et al. Composite quasar spectra from the Sloan Digital Sky Survey. *AJ* **122**, 549–564 (2001).
161. Groves, B. A., Dopita, M. A. & Sutherland, R. S. Dusty, radiation pressure-dominated photoionization. I. Model description, structure, and grids. *ApJs* **153**, 9–73 (2004).
162. Kewley, L. J., Groves, B., Kauffmann, G. & Heckman, T. The host galaxies and classification of active galactic nuclei. *MNRAS* **372**, 961–976 (2006).
163. Shen, Y. & Liu, X. Comparing single-epoch virial black hole mass estimators for luminous quasars. *ApJ* **753**, 125 (2012).
164. Barro, G. et al. Extremely red galaxies at z = 5–9 with MIRI and NIRSpec: dusty galaxies or obscured active galactic nuclei? *ApJ* **963**, 128 (2024).
165. Volonteri, M., Habouzit, M. & Colpi, M. The origins of massive black holes. *Nat. Rev. Phys.* **3**, 732–743 (2021).
166. Portegies Zwart, S. F., Baumgardt, H., Hut, P., Makino, J. & McMillan, S. L. W. Formation of massive black holes through runaway collisions in dense young star clusters. *Nature* **428**, 724–726 (2004).
167. Dayal, P. Exploring a primordial solution for early black holes detected with JWST. *Astron. Astrophys.* **690**, A182 (2024).
168. Ziparo, F., Gallerani, S. & Ferrara, A. Primordial black holes as supermassive black holes seeds. *JCAP* **2025**, 040 (2025).
169. Madau, P. & Rees, M. J. Massive black holes as population III remnants. *ApJ* **551**, L27–L30 (2001).
170. Hirschmann, M., De Lucia, G. & Fontanot, F. Galaxy assembly, stellar feedback and metal enrichment: the view from the GAEA model. *MNRAS* **461**, 1760–1785 (2016).
171. Fontanot, F. et al. The rise of active galactic nuclei in the galaxy evolution and assembly semi-analytic model. *MNRAS* **496**, 3943–3960 (2020).
172. Munari, E. et al. Improving fast generation of halo catalogues with higher-order Lagrangian perturbation theory. *MNRAS* **465**, 4658–4677 (2017).
173. Banik, N., Tan, J. C. & Monaco, P. The formation of supermassive black holes from Population III.1 seeds. I. Cosmic formation histories and clustering properties. *MNRAS* **483**, 3592–3606 (2019).
174. McKee, C. F. & Tan, J. C. The formation of the first stars. II. Radiative feedback processes and implications for the initial mass function. *ApJ* **681**, 771–797 (2008).
175. Pezzulli, E., Valiante, R. & Schneider, R. Super-Eddington growth of the first black holes. *MNRAS* **458**, 3047–3059 (2016).
176. Pezzulli, E., Volonteri, M., Schneider, R. & Valiante, R. The sustainable growth of the first black holes. *MNRAS* **471**, 589–595 (2017).
177. Zhu, Q. et al. The formation of the first quasars: the black hole seeds, accretion, and feedback models. *MNRAS* **514**, 5583–5606 (2022).
178. Sassano, F., Capelo, P. R., Mayer, L., Schneider, R. & Valiante, R. Super-critical accretion of medium-weight seed black holes in gaseous proto-galactic nuclei. *MNRAS* **519**, 1837–1855 (2023).
179. Hoyle, F. & Lyttleton, R. A. The effect of interstellar matter on climatic variation. *Proc. Camb. Philos. Soc.* **35**, 405 (1939).
180. Bondi, H. & Hoyle, F. On the mechanism of accretion by stars. *MNRAS* **104**, 273 (1944).
181. Bondi, H. On spherically symmetrical accretion. *MNRAS* **112**, 195 (1952).
182. Bhowmick, A. K. et al. Probing the $z \gtrsim 6$ quasars in a universe with IllustrisTNG physics: impact of gas-based black hole seeding models. *MNRAS* **516**, 138–157 (2022).
183. Ni, Y., Di Matteo, T. & Feng, Y. Not all peaks are created equal: the early growth of supermassive black holes. *MNRAS* **509**, 3043–3064 (2022).
184. Valentini, M., Gallerani, S. & Ferrara, A. Host galaxies of high-redshift quasars: SMBH growth and feedback. *MNRAS* **507**, 1–26 (2021).
185. Lupi, A., Quadri, G., Volonteri, M., Colpi, M. & Regan, J. A. Sustained super-Eddington accretion in high-redshift quasars. *Astron. Astrophys.* **686**, A256 (2024).
186. Massonneau, W., Volonteri, M., Dubois, Y. & Beckmann, R. S. How the super-Eddington regime regulates black hole growth in high-redshift galaxies. *Astron. Astrophys.* **670**, A180 (2023).
187. Tripodi, R. et al. HYPERION: coevolution of supermassive black holes and galaxies at z > 6 and the build-up of massive galaxies. *Astron. Astrophys.* **689**, A220 (2024).
188. Harikane, Y. et al. A JWST/NIRSpec first census of broad-line AGNs at z = 4-7: detection of 10 faint AGNs with M_{BH} 10^6–10^8 $M_\odot$ and their host galaxy properties. *ApJ* **959**, 39 (2023).
189. Kocevski, D. D. et al. Hidden little monsters: spectroscopic identification of low-mass, broad-line AGNs at z > 5 with CEERS. *ApJ* **954**, L4 (2023).
190. Ding, X. et al. Detection of stellar light from quasar host galaxies at redshifts above 6. *Nature* **621**, 51–55 (2023).
191. Kormendy, J. & Ho, L. C. Coevolution (or not) of supermassive black holes and host galaxies. *Annu. Rev. Astron. Astrophys.* **51**, 511–653 (2013).
192. Greene, J. E., Strader, J. & Ho, L. C. Intermediate-mass black holes. *ARAA* **58**, 257–312 (2020).

Acknowledgements
R.T., M.B., N.M., V.M., A.H., G.R., J.J., and G.F. acknowledge support from the ERC Grant FIRSTLIGHT and from the Slovenian national research agency ARIS through grants N1-0238, P1-0188 and the program HST-GO-16667, provided through a grant from the STScI under NASA contract NAS5-26555. This research was enabled by grant 18JWST-GTO1 from the Canadian Space Agency, and Discovery Grants from the Natural Sciences and Engineering Research Council of Canada to M.S., R.A., and A.M. Y.A. is supported by a Research Fellowship for Young Scientists from the Japan Society of the Promotion of Science (JSPS) and by the JSPS International Leading Research (ILR) project (KAKENHI Grant Number JP22K21349).

Author contributions
R.T. led the writing of this paper, performed the analysis of the spectrum, and derived the majority of the physical quantities discussed in this work. R.T., Y.A., C.W., G.D., contributed to the target selection. C.W., N.M., V.S., G.B. contributed to reduce the images. G.S., Y.A., A.M., C.W. contributed to the photometry measurements. C.W., G.B. contributed to reduce the NIRSpec data. G.S. contributed to the psf-matching. N.M. contributed to the `galfit` modeling. R.T., N.M., V.M., M.Br., F.D.E., C.W., R.M., G.G., A.H. contributed to the analysis and discussion of the spectro-photometric spectral energy distribution modeling. R.T., F.D.E., M.C. contributed to the discussion of the gas properties of the target. F.D.E. contributed to the comparison with photoionization models. MC contributed to the estimate of the metallicity of the target. R.T., N.M., V.M. contributed to the discussion of the obscuration of the target. F.D.M., S.G., V.C., M.B., J.S., contributed to the comparison with simulations and semi-analytical models. G.R. contributed to the lensing modeling and the estimate of the target magnification. J.J. contributed to the size estimate of the target. N.M., V.M., M.Br., V.C., F.D.E., C.W., F.D.M., G.R., J.S., J.J. contributed to editing the paper. A.H., G.D., M.S., I.G., A.M., G.N., G.S., R.A., Y.A., G.F., S.F., K.I., V.S., V.E.C., L.M. provided comments on the physical interpretation of the results. All authors reviewed the manuscript.

Competing interests
The authors declare no competing interests.

Additional information
Supplementary information The online version contains supplementary material available at https://doi.org/10.1038/s41467-025-65070-x.

Correspondence and requests for materials should be addressed to Roberta Tripodi.

Peer review information *Nature Communications* thanks Joseph Silk, and the other, anonymous, reviewers for their contribution to the peer review of this work. A peer review file is available.

Reprints and permissions information is available at http://www.nature.com/reprints

Publisher's note Springer Nature remains neutral with regard to jurisdictional claims in published maps and institutional affiliations.

Open Access This article is licensed under a Creative Commons Attribution-NonCommercial-NoDerivatives 4.0 International License, which permits any non-commercial use, sharing, distribution and reproduction in any medium or format, as long as you give appropriate credit to the original author(s) and the source, provide a link to the Creative Commons licence, and indicate if you modified the licensed material. You do not have permission under this licence to share adapted material derived from this article or parts of it. The images or other third party material in this article are included in the article's Creative Commons licence, unless indicated otherwise in a credit line to the material. If material is not included in the article's Creative Commons licence and your intended use is not permitted by statutory regulation or exceeds the permitted use, you will need to obtain permission directly from the copyright holder. To view a copy of this licence, visit http://creativecommons.org/licenses/by-nc-nd/4.0/.

© The Author(s) 2025